UCRL-9749
Physics Distribution
TID-4500 (16th Ed.)

UNIVERSITY OF CALIFORNIA
Lawrence Radiation Laboratory
Berkeley, California

Contract No. W-7405-eng-48

ELASTIC AND CHARGE-EXCHANGE SCATTERING OF K^- MESONS IN HYDROGEN

Ronald Rickard Ross

(Ph. D. Thesis)

June 21, 1961

DISCLAIMER

This document was prepared as an account of work sponsored by the United States Government. While this document is believed to contain correct information, neither the United States Government nor any agency thereof, nor the Regents of the University of California, nor any of their employees, makes any warranty, express or implied, or assumes any legal responsibility for the accuracy, completeness, or usefulness of any information, apparatus, product, or process disclosed, or represents that its use would not infringe privately owned rights. Reference herein to any specific commercial product, process, or service by its trade name, trademark, manufacturer, or otherwise, does not necessarily constitute or imply its endorsement, recommendation, or favoring by the United States Government or any agency thereof, or the Regents of the University of California. The views and opinions of authors expressed herein do not necessarily state or reflect those of the United States Government or any agency thereof or the Regents of the University of California.

ELASTIC AND CHARGE-EXCHANGE SCATTERING OF K^- MESONS IN HYDROGEN

Contents

Abstract vi

I. Introduction 1

II. Experimental Procedure

A. Beam 3

B. Scanning 3

C. Sketching and Measuring 5

D. Data Processing 6

1. Reconstruction of an event 6

2. Kinematical Fitting 8

3. Examination and Summary 8

4. Library 9

E. Fiducial Volume 9

III. Analysis of Events

A. Pathlength 10

B. Elastic Scattering 10

C. Charge-Exchange Scattering 18

D. Summary of Cross Sections 27

IV. Discussion of Results

A. Determination of s-Wave Zero-Effective-Range Parameters 29

B. Coulomb Nuclear Interference 41

V. Conclusions 44

Acknowledgments 45

Appendices

A. The Use of Experimental Distributions of χ^2 and the "Stretch" Quantities S_1 to Study the Uncertainties in the Observed Variables 46

B. The Distribution of Pathlength as a Function of Momentum 55

1. "True" Momentum Distribution of K^- Mesons Entering the Fiducial Volume 56
2. Pathlength as a Function of Momentum 58
C. Variance-Covariance Matrices for the Cross Sections . 63
References 72

ELASTIC AND CHARGE-EXCHANGE SCATTERING OF K^- MESONS IN HYDROGEN

Ronald Rickard Ross

Lawrence Radiation Laboratory
University of California
Berkeley, California

June 21, 1961

ABSTRACT

Cross sections for elastic and charge-exchange scattering of K^- mesons incident on hydrogen are reported at 25-Mev/c intervals from 100 Mev/c to 275 Mev/c (Table III). These cross sections are combined with the cross sections for charged- and neutral-hyperon production and the at-rest hyperon-production ratios to determine the s-wave zero-effective-range parameters that best fit the low-energy K^--p interactions. Two sets of parameters were found that give acceptable fits to all the data (Table V). The χ^2 test gives probability of 48% for Solution 1, and 8% for Solution 2. Analysis of the elastic-scattering angular distribution, independent of the zero-effective-range analysis, shows that the nuclear part of the amplitude has a large imaginary part and real part consistent with zero. Values of modulus and phase of this amplitude for the two intervals in P_K lab from 100 Mev/c to 175 Mev/c and from 175 Mev/c to 250 Mev/c are given (Table VII).

I. INTRODUCTION

The systematic study of K^--proton interactions was begun in 1956 when partially separated beams of K^- particles became available at the Berkeley Bevatron. The K^--to-background ratio at this time was roughly 10^{-3}. Original publications dealt with relatively small numbers of K^- mesons and revealed mainly the types of interactions that take place. At low momenta the following interactions were observed:

$$K^- + p \rightarrow K^- + p \quad \text{Elastic}$$
$$\bar{K}^0 + n \quad \text{Charge exchange}$$

- -

$$\left.\begin{array}{l} \Sigma^- + \pi^+ \\ \Sigma^0 + \pi^0 \\ \Sigma^+ + \pi^- \\ \Lambda + \pi^0 \\ \Lambda + 2\pi \end{array}\right\} \quad \text{Hyperon production}$$

All these interactions conserve charge, strangeness, isotopic spin, and baryon number. To date, no other interactions have been observed (at low momenta).

The determination of cross sections as a function of momentum became feasible only after considerable improvements had been made in techniques used for separating K^- mesons from other particles. Early in 1958, a beam in which the K^--to-background ratio was about 10^{-2} was constructed. This report on the elastic and charge-exchange scattering of K^- mesons in hydrogen is based on exposure of the Berkeley 15-inch hydrogen bubble chamber to this enriched beam. The total number of K^- mesons entering the chamber was approximately 11,000.

This work forms a part of the large effort by bubble chamber and emulsion researchers to accumulate experimental data on the $\bar{K}$-N interactions. Freden, Gilbert, and White have recently summarized the previously published results on K^--proton interactions.[1] Their paper contains references to work by emulsion and bubble chamber groups. The data that we report here have been reported previously in preliminary form.[2,3] Data on hyperon production—contained in the same film as the elastic- and charge-exchange scattering data—have been handled by techniques similar to those discussed in this paper, but are the subject of a separate report.[4]

Section II of this paper is devoted to the explanation of those experimental procedures pertinent to the experiment as a whole. In Section III, methods and techniques of analysis peculiar to the individual event types are explained and experimental results for each type are presented. Finally, Section IV is devoted to a discussion of these results and their relation to available theory.

II. EXPERIMENTAL PROCEDURE

A. Beam

The main problem encountered in setting up a K^- beam at the Bevatron is the separation of the K^- mesons from the π^- background. This is difficult in that the π^--to-K^- production ratio is about 1000 to 1 at a secondary beam momentum of 450 Mev/c. Since the π^- mesons live longer than the K^- mesons, this ratio becomes even larger at the detector. In this experiment, the problem was solved by using a co-axial velocity spectrometer developed at Berkeley by Joseph J. Murray.[5] The resulting beam has been described in detail elsewhere,[6] so that only its characteristics at the bubble chamber are given here.

A schematic diagram of the beam is shown as Fig. 1. The momentum before the absorber was 425 Mev/c and the thickness of the copper absorber was adjusted to give a mean momentum of approximately 180 Mev/c at the center of the chamber. Because of the nonlinear nature of the range-momentum relationship, the momentum distribution at the chamber was very skew.

The flux of K mesons was 1 in four pictures. It was limited mainly by the number of background tracks allowed per picture, which was nominally 25. The background consisted of 85% μ^- and e^- and 15% π^-. In a total of about 45,000 pictures, we observed approximately 11,000 K^- mesons that either passed through or interacted within the chamber.

B. Scanning

The scanning procedure was based on the fact that the K^- mesons could be distinguished from the background tracks by means of their ionization and curvature. For all momenta in the beam, the K^- tracks were more than twice minimum ionizing. The background consisted mostly of minimum-ionizing tracks; the exceptions, those background tracks having low enough velocity to be as heavily ionizing as K^- mesons, were much more curved in the magnetic field than a stopping K^- meson would be. These evidences allowed us to identify

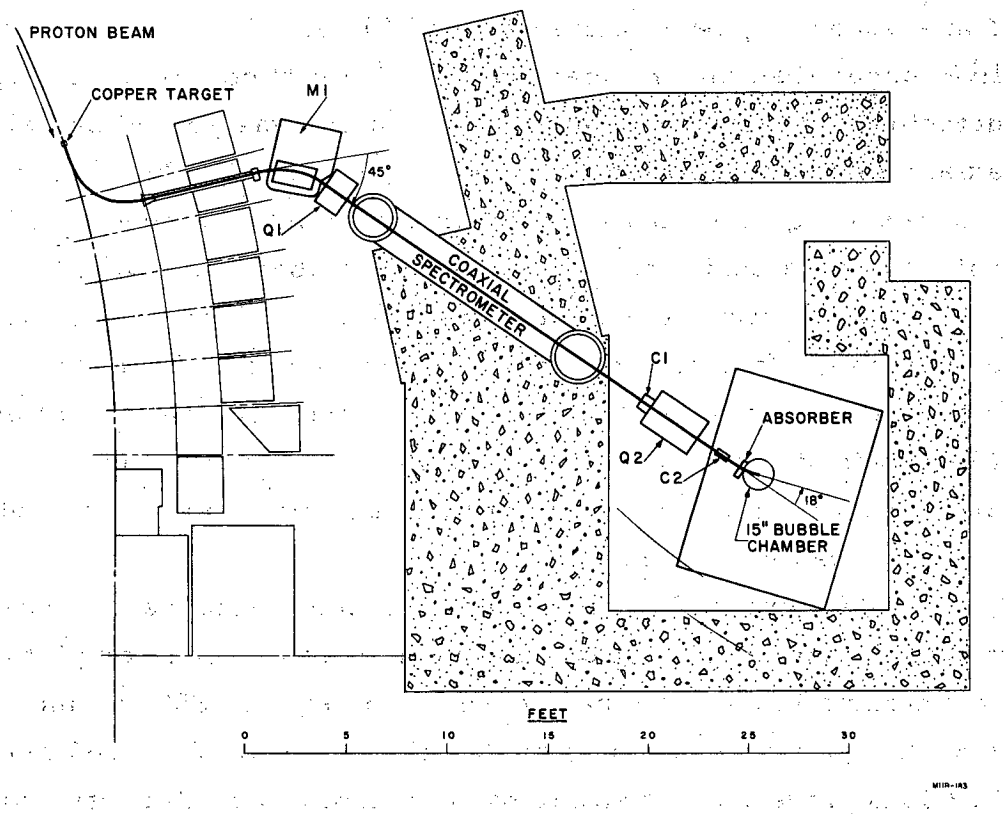

Fig. 1. Schematic diagram of the 450-Mev/c K^- beam at the northwest target area of the Berkeley Bevatron.

a sample of K^- mesons independently of what happened to them in our fiducial volume. The first quarter of each frame (the UP region) was set aside for identifying the K^-, and the rest of the picture (the IN region) was used to study the interactions.

The procedure was as follows: with the IN region masked from view, the scanner examined the UP region and recorded the number of densely ionizing tracks. The "IN" region was then unmasked and the scanner noted whether the dense tracks interacted, decayed, passed through the chamber, or were too curved. Those not too curved were assumed to be K^- mesons. The interactions and decays were recorded according to the final state of the system when this could be easily identified. There were special classes for events having ambiguous interpretations, such as "$\Sigma^{\pm}$" when the Σ particle decayed before going far enough to be observed and "K_ρ" when the final state consisted of neutral particles with the unstable ones decaying via neutral modes. A K^- meson going all the way through the chamber was recorded as "KGT" (K-Go-Through).

C. Sketching and Measuring

To aid the measurer in finding the identifying the particle tracks, a sketch was made of each event. The sketch also indicated in which two of the four possible views each track was to be measured. The identification of the event was checked and each event was given a code number according to its type, and this code word was used to assign masses to the tracks in subsequent computer programs. Finally, each frame having a K_ρ event (see Sec. II-B) was again scanned for decays of neutral particles.

The measurements were made on a projection microscope (Franckenstein) with the information punched on IBM cards which served as input to the data-processing system.

D. Data Processing

The data were processed by a series of computer programs written for the IBM 704 and 709 digital computers. The steps involved in the system are shown in the block diagram of Fig. 2 and are briefly described below.

1. Reconstruction of an Event

The first step is accomplished by the program PANG, written for the IBM 704 and 709 digital computers.[7] An event is processed one track at a time, input consisting of the points measured along the track, measurements of two fiducial marks for each view, and the event-type code. Geometrical optics is used to construct space points along the track.

The x, y plane of the space points has its normal approximately along the magnetic field lines in the chamber, and is therefore the plane used to determine the momentum of the track. The x, y projections of the space points are fitted with a parabola. We use the momentum estimated from the curvature of this parabola, plus the mass, the range-momentum relationship, and the magnetic field as a function of chamber position, to calculate the second derivative of the track at two points. The final x, y fit is a fourth-order polynomial satisfying the constraints on the second derivative at those points. The final fit in the z direction is a third-order polynomial taking into account the horizontal component of the magnetic field. The parameters of these polynomials are used to compute the momentum at the center of the track, the directions at both ends, and the length. The momenta at both ends of the track are calculated by using the momentum-at-center and the range-momentum relationship. For particles that stop in the chamber, the momentum is determined from the measured range of the track. Uncertainties in momenta and angles due to multiple Coulomb scattering, range straggling, and measurement uncertainties are also computed. Finally, the output of PANG for each event is written in the binary mode on an intermediate magnetic tape for input to the next step in the data processing.

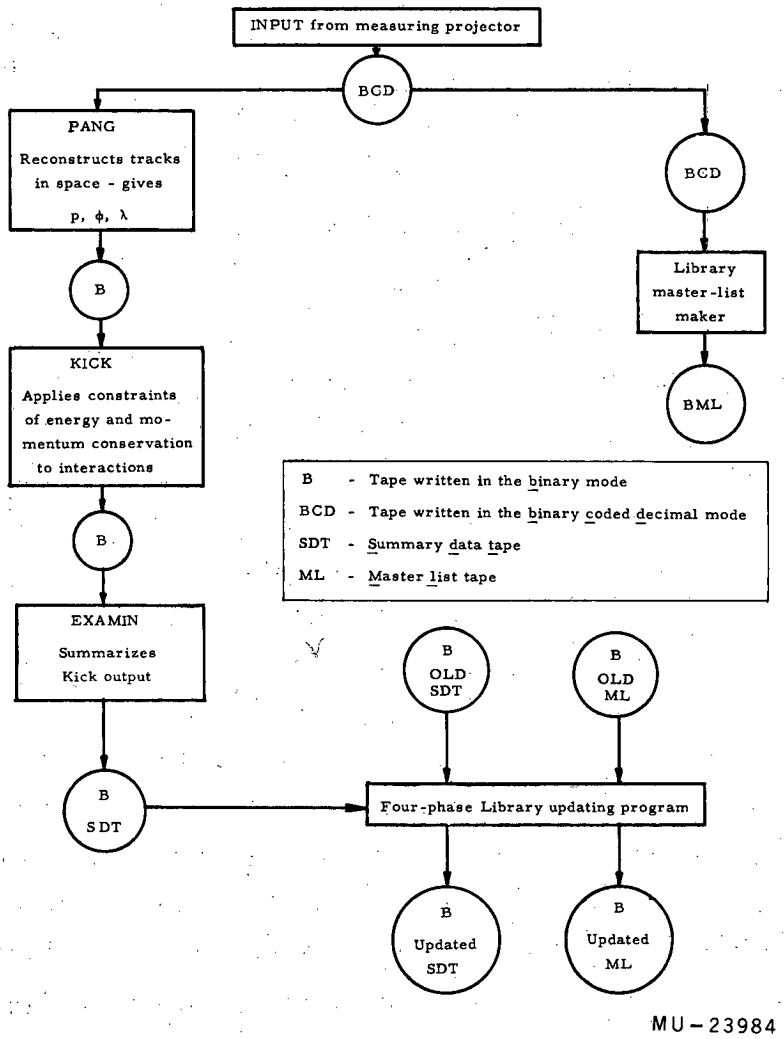

Fig. 2. Block diagram of the system of computer programs used for the analysis of K^--p interactions in this experiment.

2. Kinematical Fitting

The computer program KICK is designed to apply constraints of momentum and energy conservation to an event.[8] It uses the method of least squares with constraints. The parameters of the problem correspond to adjusted values of the measured variables. The method picks, from all possible sets of parameters satisfying the equations of constraint, that set which minimizes the value of χ^2, where χ^2 is defined as

$$\chi^2 = \sum_{\substack{i=1 \\ j=1}}^{N} (x_i - x_i^m) G_{ij} (x_j - x_j^m) .$$

In this equation, the x_i are the parameters, x_i^m are the measured variables, and G is the inverse of the variance-covariance matrix of the measured variables.

The output of KICK consists of the adjusted values of the parameters and their variance-covariance matrix. In addition, the final value of χ^2 and normalized "stretch" quantities, $S_i(x)$, on each measured variable are given. If proper uncertainties have been assigned, χ^2 provides a measure of the goodness of fit, and the normalized "stretch" quantities are normally distributed with a mean value 0 and standard deviation 1. Departures from these conditions indicate erroneous uncertainty assignments. The distribution of χ^2 gives information regarding the over-all fit, whereas the distribution of S_i gives information on the individual variables x_i^m. Data on the distributions of χ^2 and "stretch" quantities are given in Appendix A.

3. Examination and Summary

The KICK output serves as input for the EXAMIN program whose main function is to sort good information from the KICK output and put it on a "data-summary" tape. The identification and nature of failure for events not processed successfully are also recorded on this tape in brief form.

4. Library

A master list of all events in this experiment was put on magnetic tape. The output of EXAMIN was used to update information on this master list, and also to update data summary tapes containing previously accepted events. The updated library tape then served as a source for lists of events that had not yet been handled, and a history of why they had failed previously. We set up an analogous system to determined, pathlength. In this case, the master list and data summary were on the same tape. The data-summary tapes and master lists were the final source of information used for the analysis.

E. Fiducial Volume

For the analysis, we used only events and path length within a specified volume of the chamber (the fiducial volume). The boundaries of this volume were chosen so that: the interactions were clearly visible in all four views; the escape correction for unstable neutral particles was small; the volume was entirely within the IN region; and the volume was as large as possible subject to the above conditions. On input to the KICK program, a test was made on each event to determine whether or not it was in the volume.

III. ANALYSIS OF EVENTS

A. Pathlength

The total K^- pathlength was 1600 meters—or nearly 1 mile—of which 64.2% was contributed by KGT tracks, 29.2% by K mesons that stopped or interacted, and 6.6% by K mesons that decayed. The total length was obtained by measuring the length (within the fiducial volume) of each track. Figure 3 shows the distribution of this pathlength as a function of momentum. The method we used to determine this distribution is discussed in Appendix B.

B. Elastic Scattering

A total of 419 elastic scatterings were observed within the fiducial volume. Selection criteria on the minimum angle of scattering and minimum momentum were applied to these events to obviate large and uncertain corrections to the data. The small-angle cutoff was made on the cosine of the center-of-mass (c.m.) angle, in order to have all angular distributions over the same range of $\cos\theta_{c.m.}$. The cutoff was $\cos\theta_{K\,c.m.} = 0.966$, which corresponds to a laboratory-system scattering angle for the K^- of approximately 10 deg over the entire momentum range. For momenta less than 200 Mev/c, the amplitude for Coulomb scattering at this angle is larger than the nuclear amplitude, and the effect of the Coulomb nuclear interference is clearly indicated by the data. At higher momenta, the Coulomb nuclear interference has less effect on the angular distribution because the maximum interference is at an angle smaller than the cutoff.

Additional selection criteria were applied to the azimuthal angle of the plane of the scattering for events with $\cos\theta_{c.m.}$ between 0.966 and 0.85. Events in this range whose plane of scattering made an angle greater than 30 deg with a vertical plane were accepted. Five events failed this criterion, whereas azimuthal symmetry predicts (from events satisfying the criterion) that 13.5 events should fail. A correction of 3/2 (based on the assumption of azimuthal symmetry) was applied to the events accepted. The events left after application of the small-angle and azimuthal-angle cutoffs are shown in Fig. 4.

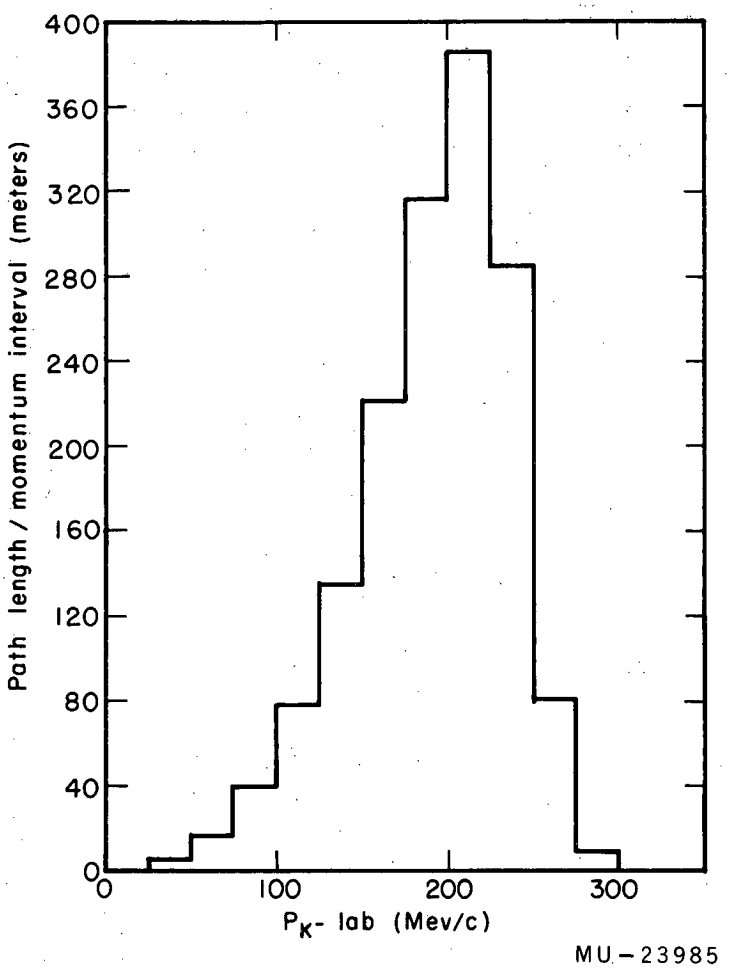

Fig. 3. K^- pathlength as a function of K^- momentum (lab).

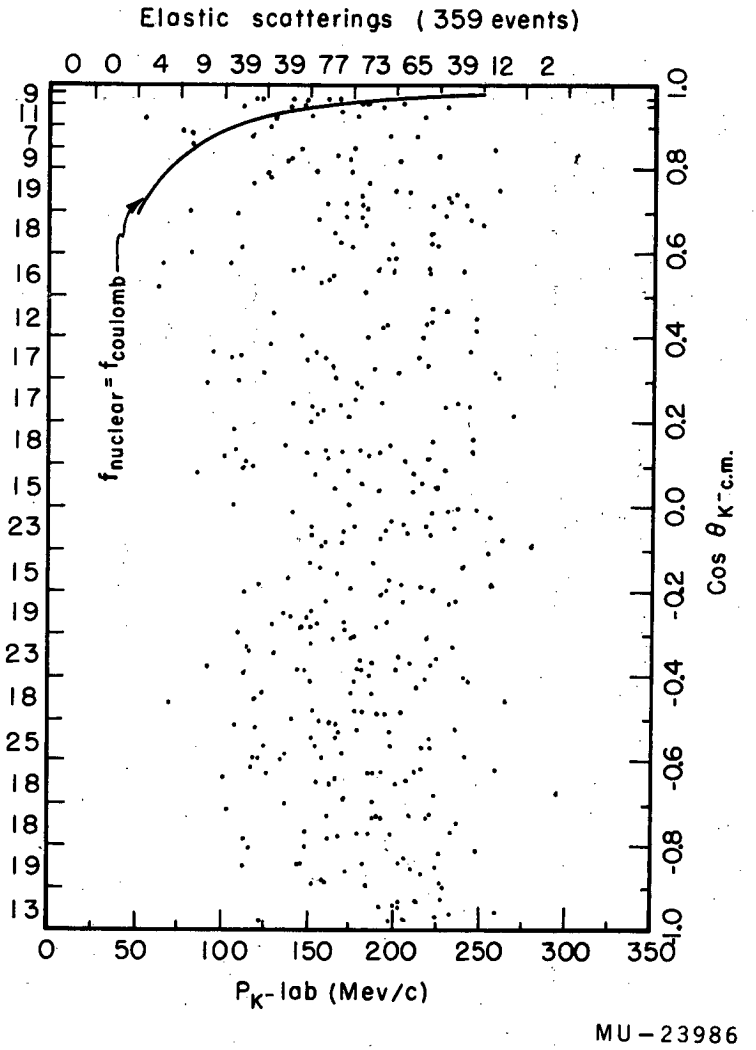

Fig. 4. Scatter plot of observed elastic scatterings that satisfy the selection criteria applied. No selection criteria are applied to events with $\cos\theta_{c.m.} > 0.85$. The numbers of events in both momentum and $\cos\theta$ bands are indicated on the sides opposite the scales.

A K^- laboratory-system momentum cutoff at 100 Mev/c was imposed for the following two reasons:

(a) The detection efficiency for elastic scatterings is a function of the length of the recoil particles, and therefore decreases rapidly at low momenta. K^- mesons of 100 Mev/c have a residual range in liquid hydrogen of a little over 1.5 cm. When they scatter at 180 deg from a proton they are left with a residual range of 0.2 mm, which is not enough to make 1 bubble (1 bubble $\approx$ 0.25 mm); however, the proton has a range of 0.7 cm and is easily detected. At 75 Mev/c the residual range of the K^- is down to 0.5 cm, and the corresponding 180-deg scattering produces a proton with a range of about 3 mm. In scatterings at angles less than 180 deg at these momenta, both proton and K^- tracks are very short. Because of the short recoil tracks, we must take into account that a K^- meson coming to rest in liquid hydrogen makes charged hyperons more than half the time. Pictures of this type of event have two densely ionizing tracks and one light one, all meeting at a point. The charged hyperon and π meson are collinear, but have random orientation with respect to the K^- direction. There is, therefore, some probability that the elastic scatterings at low momenta preceding this type of event will be obscured.

(b) The other effect that requires a 100-Mev/c cutoff is the distortion of track images caused by nonuniform density of liquid hydrogen in the light path from track to film. We observed displacements of the images of tracks by as much as a track width over lengths of track from 1 mm to 0.5 cm. The effect could be compensated for if it were in the middle of a long track, but those cases in which the distortion was in the last 0.5 cm of the incident K^- were very difficult to interpret. These factors, giving rise to large uncertainties in scanning biases at low momenta, coupled with the fact that only 13 events are observed between 50 and 100 Mev/c, made it necessary to apply this cutoff at 100 Mev/c in order to determine cross sections.

Two sources of systematic error in the number of events observed at small angles were considered. The first concerns an enhancement of the number of large-angle events observed owing to uncertainty in the value of the measured angle of scattering. Since individual measurements of the angle of scattering are, to first approximation, distributed symmetrically about the true angle of scattering, and since uncertainty of measurement does not vary rapidly with angle, the probability of observing a 9-deg scattering at 11 deg is the same as the probability of observing an 11-deg scattering at 9 deg. However, the $\left[1/\sin^4(\theta/2)\right]$ dependence of the Coulomb cross section gives more events truly at 9 than at 11 deg, and so the number observed at 11 deg is systematically increased. Corrections for this effect were calculated on the assumption that the angular distribution is given by the Coulomb cross section out to angles where the Coulomb cross section is equal to the nuclear cross section. No corrections were applied beyond this angle.

The second source of systematic error considered was that due to Molière or plural scattering. For the angles considered, Molière scattering can be represented as an effective increase in the Coulomb scattering cross section. Bethe has derived a formula for the asymptotic ratio of Coulomb to actual scattering,[9] and calculations of this ratio for pathlength of 0.5 cm of liquid hydrogen showed the effect to be small. The largest correction was 2%.

The final corrections applied to the elastic scattering events are shown in Table I. Recall that from $\cos\theta = 0.966$ to $\cos\theta = 0.85$, a factor of 1.5 must be applied because of the azimuthal-angle cutoff. This factor, 1.5, has been slightly modified to take into account the two corrections just mentioned: (a) uncertainty in measured angle, and (b) Molière scattering. No corrections were necessary in the region -1.0 to 0.85 in $\cos\theta_{c.m.}$

Table I

Correction applied to maximum likelihood estimates of elastic scatterings shown in Fig. 5

$\cos\theta_{c.m.}$ Interval	Momentum interval (Mev/c)						
	100-125	125-150	150-175	175-200	200-225	225-250	250-275
0.95 to 0.966	1.25	1.37	1.38	1.38	1.50	1.50	1.50
0.90 to 0.95	1.35	1.42	1.50	1.50	1.50	1.50	1.50
0.85 to 0.90	1.50	1.50	1.50	1.50	1.50	1.50	1.50
-1.0 to 0.85			No corrections (1.0)				

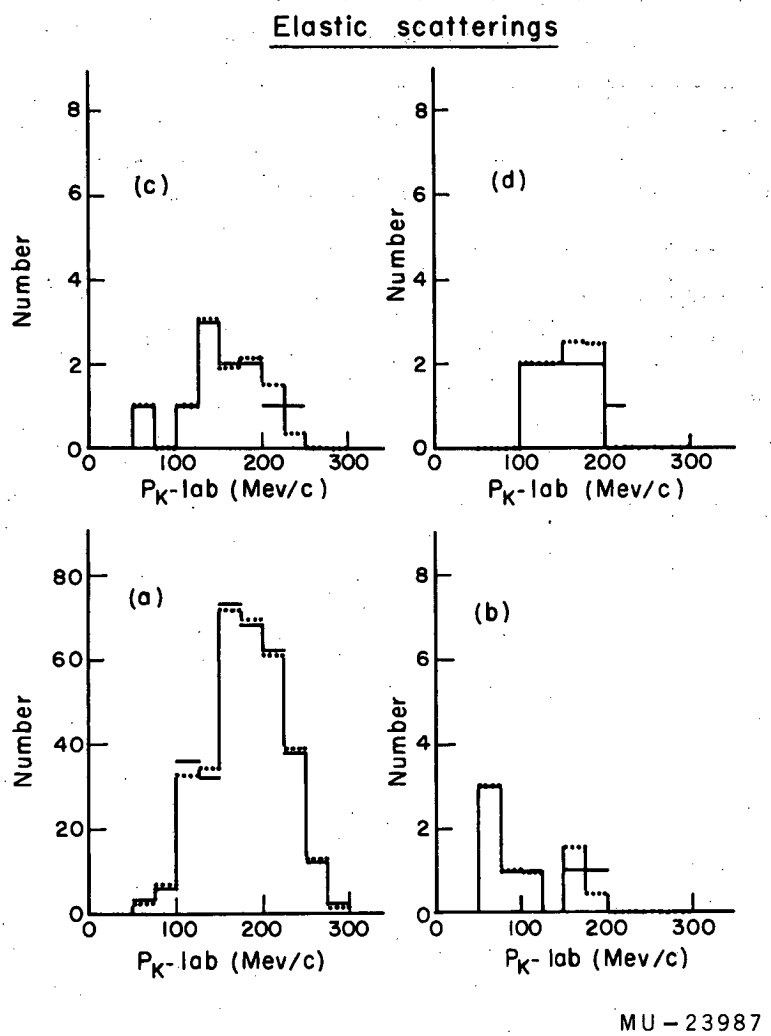

Fig. 5. Histograms of the numbers of observed scatterings (solid lines) and the maximum-likelihood estimates of the distribution of these events (broken lines) as a function of K^- momentum (lab) for the four intervals of $\cos\theta_{K^- \text{c.m.}}$:

(a) -1.0 to 0.85, (b) 0.85 to 0.90,
(c) 0.90 to 0.95 and (d) 0.95 to 0.966.

Table I contains corrections to apply to the maximum-likelihood estimates of this figure to obtain the total number of scatterings.

To determine cross sections as a function of momentum and angle, the events of Fig. 4 were divided into four intervals in $\cos\theta_{c.m.}$ and ten intervals in momentum. Because of the isotropic nature of the distribution in the region where Coulomb scattering is small ($\cos\theta_{c.m.}<0.85$), the data in this region were all lumped into one $\cos\theta$ interval. The three intervals in $\cos\theta_{c.m.}$, 0.85 to 0.90, 0.90 to 0.095, and 0.95 to 0.966, were chosen to give a maximum amount of information about the Coulomb nuclear interference. In the choice of momentum-interval widths, we were guided by the desire to measure the cross section as a function of momentum as accurately as possible. An interval covering all events of the experiment would give an accurate measurement of the average cross section because of the large number of events, but would give no information about the momentum dependence of the cross section. On the other hand, if the intervals were too narrow, the statistical fluctuations of the numbers of events in the individual bins would be large, and uncertainty in the momentum of individual events would cover several bins. The 25-Mev/c width used was a compromise between the two extremes. The events in each angular region were analyzed separately as a function of momentum. To allow for the uncertainty in K^- momentum of the individual events, we used the maximum-likelihood method to estimate the number of events in each of ten momentum intervals, starting at 50 Mev/c. Details on the formulation of the likelihood function are given in the thesis of William E. Humphrey.[4] Figure 5 shows the observed numbers of events as a function of momentum (solid lines) and the maximum-likelihood estimates (broken lines).

The estimates for events with $\cos\theta$ greater than 0.85 were adjusted by using the correction factors in Table I. These final estimates for momentum K^- lab > 100 Mev/c were converted to cross sections by using a density of liquid hydrogen of 0.0586 g/cm^3 and the pathlength shown in Fig. 3. The elastic cross sections as a function of momentum and angle were combined with other data on the K^--p interactions to determine the parameters for an s-wave zero-effective-range theory. The method used for this determination is discussed in Sec. IV-A.

It was considered desirable to determine the modulus and phase of the nuclear part of the elastic scattering amplitude independent of the s-wave zero-effective-range theory. To get a statistically significant estimate of the scattering amplitude, we determined two average differential-scattering cross sections by averaging the cross sections for each angular region over groups of three momentum intervals. The average differential-scattering cross sections for the intervals 100 Mev/c to 175 Mev/c, and 175 Mev/c to 250 Mev/c, K^- momentum (lab) are shown in Fig. 6. In Sec. IV-B, we show how the nuclear part of the scattering amplitude has been estimated from these cross sections.

The total elastic-scattering cross section for values $\cos\theta_{c.m.}$ between -1.0 and 0.966 is shown in Fig. 7 as a function of K^- momentum (lab). These values are the sums of cross sections observed in the four angular intervals, and therefore contain Coulomb as well as nuclear scattering. The uncertainties are the square root of the diagonal terms of the variance-covariance matrix, obtained by summing the matrices for the cross sections in the four angular intervals. More detail on the variance-covariance matrix for the cross sections is given in Appendix C. The solid curve is the cross section calculated from Eq. (3.1) by using the parameters of solution 1 in Table V.

C. Charge-Exchange Scattering

A $\overline{K}^0$ production event is detectable when the $\overline{K}^0$ decays via one of its charged modes, or when it interacts in the hydrogen in such a way as to produce charged particles. Of the 29 $\overline{K}^0$ events observed, 25 were normal K_1^0 decays,

$$K_1^0 \rightarrow \pi^+ + \pi^- ,$$

and formed the sample used for calculation of the cross section as a function of momentum. In addition, there were two inelastic scatterings giving rise to hyperons. The first scattering was identified as

$$\overline{K}^0 + p \rightarrow \Sigma^+ + \pi^0 ,$$

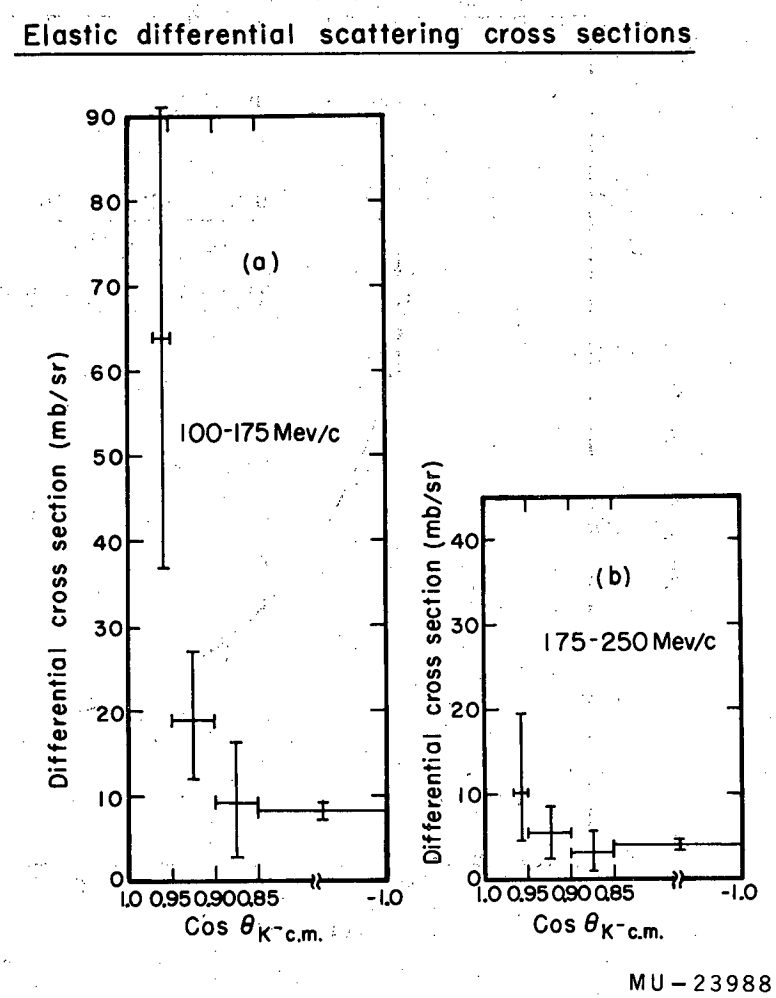

Fig. 6. K^-p elastic differential scattering cross section:
(a) 100 Mev/c $\leqslant P_{K^-}$lab $\leqslant$ 175 Mev/c, and
(b) 175 $< P_{K^-}$lab $\leqslant$ 250 Mev/c.

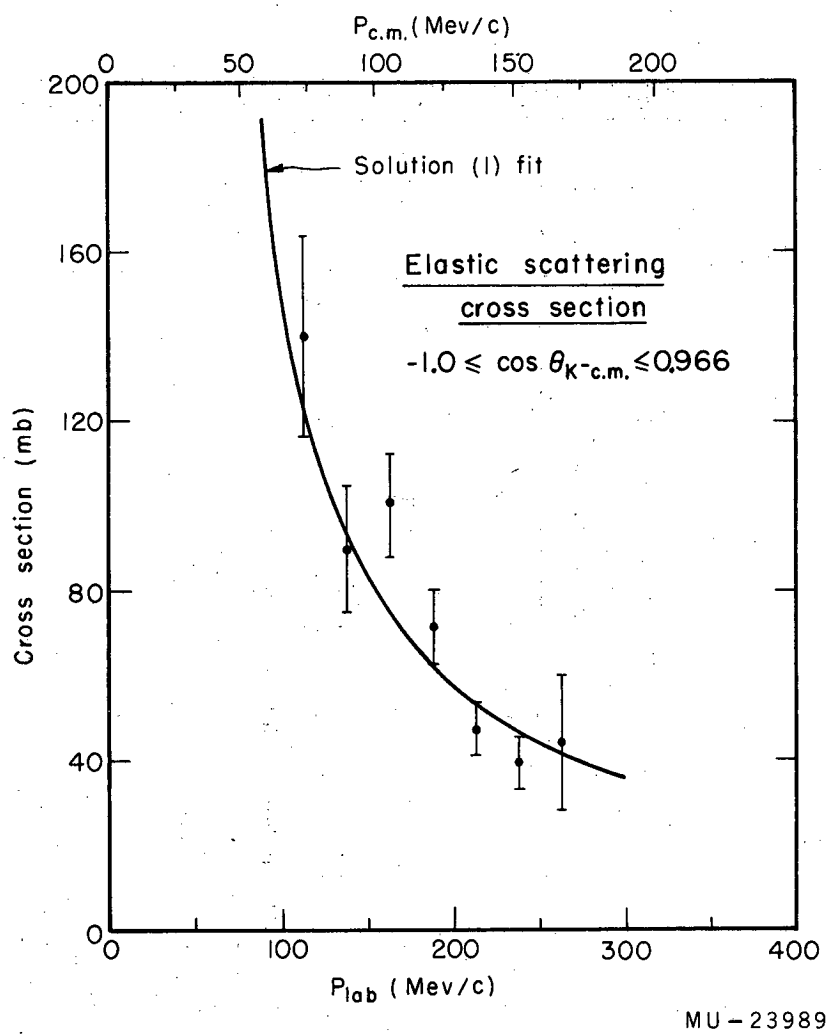

Fig. 7. Total K^--p elastic-scattering cross section for $\cos\theta_{K^-c.m.}$ between -1.0 and 0.966 as a function of K^- momentum (lab). The solid curve is the intergral of Eq. (3.1) from -1.0 to 0.966 in $\cos\theta_{K^-c.m.}$, for the scattering lengths of solution 1 (Table V).

followed by $\Sigma^+ \rightarrow p + \pi^0$; the second as

$$\bar{K}^0 + p \rightarrow \Lambda + \pi^+$$

followed by $\Lambda \rightarrow p + \pi^-$.

Two other $\bar{K}^0$ events were examples of the K_2^0 decay into three-body final states. The observation of two K_2^0 decays is consistent with the published lifetime of $6.1(+1.6/-1.1)\times 10^{-8}$ sec.[10]

Care was taken to distinguish the two types of "V"s observed in this experiment; the $\bar{K}^0$ decays and the Λ-hyperon decays via the mode

$$\Lambda \rightarrow p + \pi^-.$$

Ambiguities in the identification of these V events arise only if the proton of the Λ decay cannot be distinguished from the π^+ of the K_1^0 decay. In a total of about 1000 V's, only five cases were ambiguous at the scanning stage, and a kinematical analysis of these events for both interpretations yielded unambiguous identification for all five. Three were Λ events and two were K_1^0.

We used only K_1^0 of length > 1 mm, to avoid ambiguity between events with short $\bar{K}^0$ and short Σ tracks. Since the K_1^0 lifetime is approx 10^{-10} second, a substantial fraction decays close to the production vertex. These events give rise to a π^+-π^--meson pair originating close to the end of the K^- track. It is difficult to distinguish this configuration from that of events in which a charged Σ hyperon (produced in association with a π meson of opposite charge) decays into a charged π meson and neutron after going less than 1 mm. About 300 such short Σ's were in the film. The similarity in momenta of the π's in the interactions

$$K + p \rightarrow \Sigma^{\pm} + \pi^{\mp} \qquad \Sigma^{\pm} \rightarrow \pi^{\pm} + n,$$

and

$$K^- + p \rightarrow \bar{K}^0 + n \qquad \bar{K}^0 \rightarrow \pi^+ + \pi^-,$$

makes kinematical separation impossible for many spatial configurations if the Σ or $\overline{K}^0$ track is too short to be seen. It was often possible to fit both hypotheses.

Application of the 1-mm cutoff eliminated one of the 25 detected events. For each of the remaining K_1^0's we calculated the probability of the $\overline{K}^0$ length being less than 1 mm, and the probability of escaping the volume. In this way the observed K_1^0's served as an estimate of the spatial and momentum distribution of the complete sample. The calculations indicated that 17.8% (5.25 events) should be less than 1 mm long and that 0.9% (1/3 of an event) should escape the volume. In the second column of Table II we list the corrections applied to the data for the different momentum bins. The lifetime used for these corrections was 0.95×10^{-10} sec.[10] Corrections were also made for the fact that only 1/3 of the $\overline{K}^0$'s produced decay via the charged K_1^0 mode. The third column of Table II (Col. 2 multiplied by 3.0) gives the final corrections.

In Fig. 8 we show a scatter diagram of the 25 $\overline{K}^0$ events. The χ^2 for the hypothesis of an isotropic angular distribution is 3.8 for three degrees of freedom. Figure 9 is a histogram of the number of events as a function of momentum. The solid lines represent the observed numbers obtained from the scatter plot (the circled event with length < 1 mm was removed), and the broken lines represent the maximum-likelihood estimates obtained when the uncertainties in the momenta are taken into account. Correlations between neighboring bins ranged from -9% to -17%.

Cross sections calculated from the maximum-likelihood estimates are shown in Fig. 10. The uncertainties in the cross sections are the square roots of the diagonal terms in the final variance-covariance matrix for the set of cross sections. The calculation of this matrix is discussed in Appendix C. The measured cross sections were used in determining the parameters of the s-wave zero-effective-range theory as discussed in Sec. IV-A. The solid curve in Fig. 10 is the

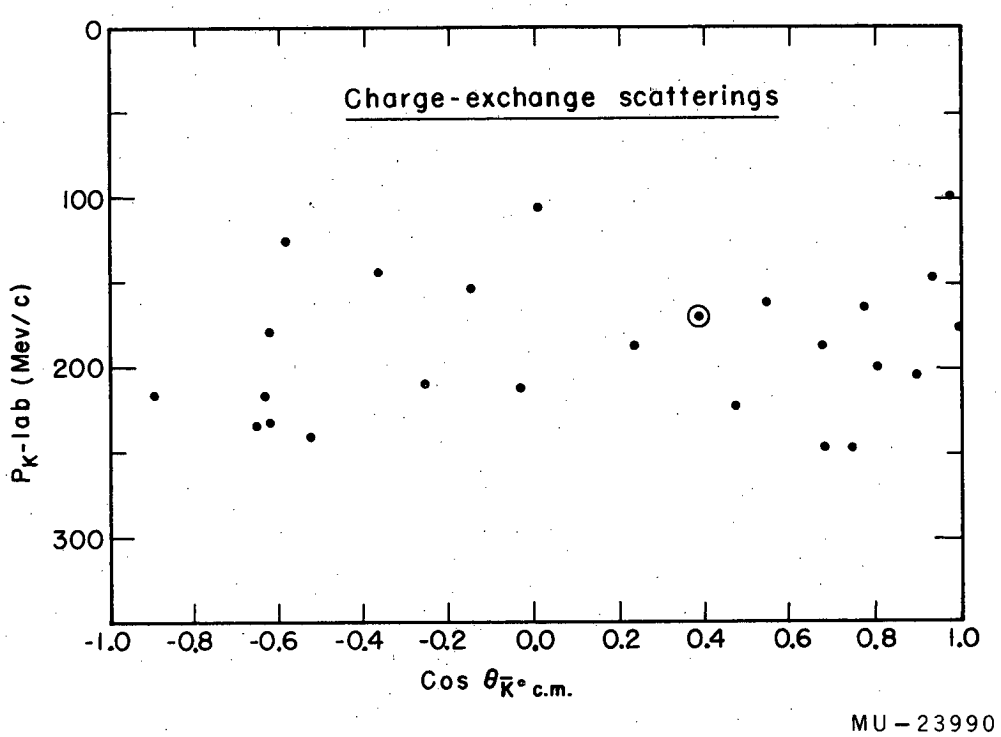

Fig. 8. Scatter plot of $\bar{K}^0$-n production events with K_1^0 decays. The circled event has a $\bar{K}^0$ length less than 1 mm.

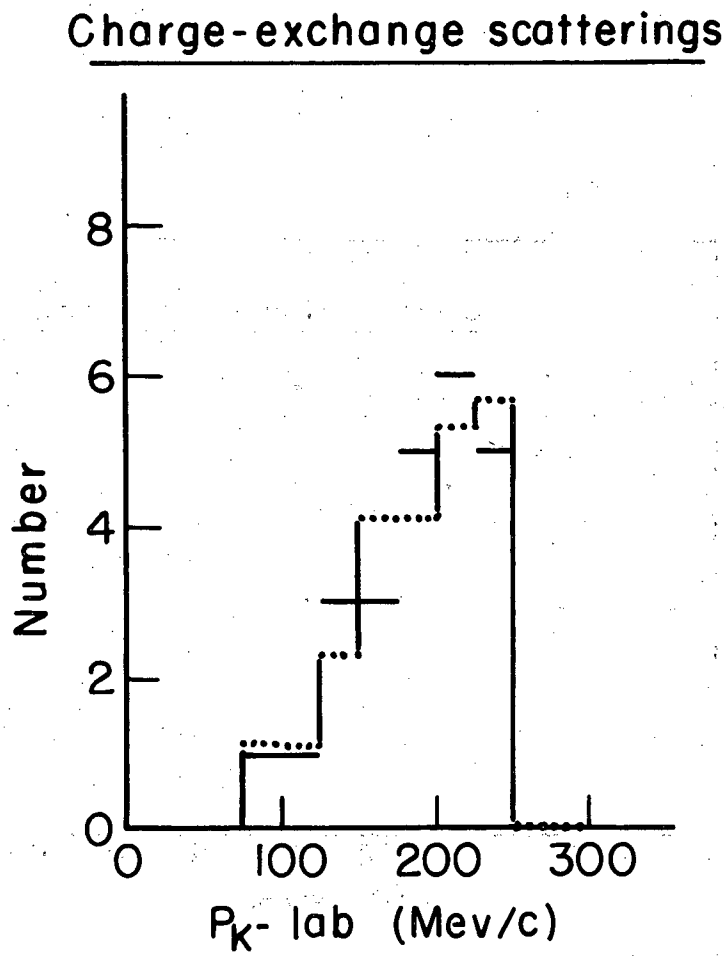

MU-23991

Fig. 9. Histograms of the numbers of observed K_1^0 decays (solid lines) and the maximum-likelihood estimates of the distribution of these events (broken lines) as a function of the incident K^- lab momentum. Table II, Col. 3, contains corrections to apply to the maximum likelihood estimates to obtain the total number of $\overline{K}^0$-n produced.

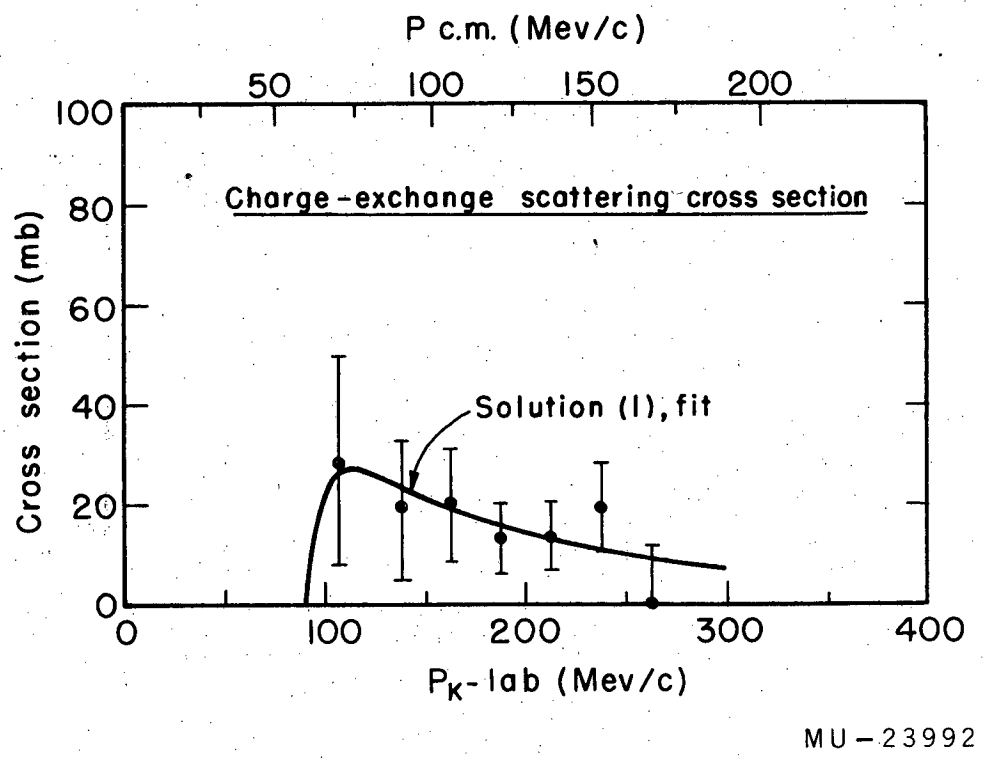

Fig. 10. K^--p charge-exchange scattering cross section as a function of K^- lab momentum. The solid curve is a graph of Eq. (3.2) for the scattering lengths of Solution 1 (Table V).

Table II

Correction applied to maximum likelihood estimates of $\overline{K}^0$-n production events shown in Fig. 9

Momentum range (Mev/c)	Correction for length < 1 mm plus escape from volume	Final correction (col. 2)×3(Non-$\pi^+\pi^-$ decay of $\overline{K}^0$)
89-100	1.40	4.2
100-125	1.50	4.5
125-150	1.30	3.9
150-175	1.27	3.8
175-200	1.16	3.5
200-225	1.16	3.5
225-250	1.14	3.4
250-275	1.14	3.4

cross section calculated from Eq. (3.2), using the parameters which give the best over-all fit to K^--p interactions (solution 1 of Table V).

D. Summary of Cross Sections

For easy reference we have listed in Table III pathlength, observed numbers of events, corrected numbers of events, and the calculated cross sections for elastic and charge-exchange scattering, as a function of the incident K^- momentum (lab). The variance-co-variance matrices, corresponding to the cross sections in this table, are given in Tables XI through XVI in Appendix C.

Table III. Summary of pathlength, observed number of events, corrected numbers, and cross sections, as a function of the incident K^- lab momentum

		Elastic Scattering															Charge-exchange scattering		
		$\cos\theta_{c.m.}$ -1.0 to 0.85			$\cos\theta_{c.m.}$ 0.85 to 0.90			$\cos\theta_{c.m.}$ 0.90 to 0.95			$\cos\theta_{c.m.}$ 0.95 to 0.966			$\cos\theta_{c.m.}$ -1.0 to 0.966					
K^- lab momentum interval (Mev/c)	Pathlength (meters)	Number observed	Corrected number	Cross section (mb)	Number observed	Corrected number	Cross section (mb)	Number observed	Corrected number	Cross section (mb)	Number observed	Corrected number	Cross section (mb)	Number observed	Corrected number	Cross section (mb)	Number observed	Corrected number	Cross section (mb)
100–125	78.40	36	32.9	120.2	1	1.5	5.5	1	1.4	4.9	2	2.5	9.0	40	38.3	139.6	2[a]	10.0[a]	28.4[a]
125–150	136.79	32	34.4	71.9	1	1.5	3.1	3	4.4	9.1	2	2.8	5.9	38	43.1	90.0	3	9.1	19.0
150–175	221.54	73	72.1	93.1	0	0	0	2	2.9	3.7	2	3.5	4.5	77	78.5	101.3	3	15.8	20.4
175–200	316.25	68	69.9	63.2	1	2.3	2.1	2	3.2	2.9	2	3.5	3.1	73	78.9	71.3	5	14.6	13.2
200–225	385.98	62	61.1	45.2	1	0.7	0.5	1	2.3	1.7	1	0	0.0	65	64.1	47.4	6	18.6	13.8
225–250	285.10	38	38.6	38.7	0	0	0	1	0.5	0.5	0	0	0.0	39	39.1	39.2	5	19.4	19.4
250–275	80.83	12	12.5	44.2	0	0	0	0	0	0	0	0	0.0	12	12.5	44.2	0	0	0

[a]The first interval for the charge-exchange scattering is for a K^- lab momentum interval from 89 Mev/c to 125 Mev/c. The pathlength for this interval was 100 meters.

IV. DISCUSSION OF RESULTS

A. Determination of s-Wave Zero-Effective-Range Parameters

The data presented in Sec. III have been combined with the hyperon-production data[4] to determine parameters for an s-wave zero-effective-range theory of the K^--p interaction. In 1958 Jackson, Ravenhall, and Wyld suggested the use of a zero-effective-range theory for parameterizing the K^--p interactions.[11] Since that time, many refinements have been made in the theory to adapt it to the K^--p system.[12, 13, 14] For instance, the K (reaction)-matrix formalism, has been introduced in order to handle charge-dependent effects related to the $\bar{K}^0$-n—K^--p mass difference without sacrificing the charge-independent nature of the nuclear matrix elements, and Coulomb effects (important at low momenta) have been included. The most recent and complete treatment has been given by Dalitz and Tuan.[14] In their notation, the equations for the cross sections given in this theory are

$$\frac{d\sigma_{el}}{d\Omega} = \left| \frac{\csc^2 \theta/2}{2Bk^2} \exp\left[\frac{2i}{kB} \ln \sin \theta/2\right] + \frac{C^2/2\left[A_0(1-ik_0A_1)+A_1(1-ik_0A_0)\right]}{D} \right|^2 ; \tag{3.1}$$

$$\sigma_{ch.ex.} = \frac{\pi k_0 C^2}{k} \left| \frac{A_0 - A_1}{D} \right|^2 ; \tag{3.2}$$

$$\sigma_0 = \frac{4\pi b_0 C^2}{k} \left| \frac{1-ik_0A_1}{D} \right|^2 ; \tag{3.3}$$

$$\sigma_1 = \frac{4\pi b_1 C^2}{k} \left| \frac{1-ik_0A_0}{D} \right|^2 ; \tag{3.4}$$

where

$$D = 1 - i\left(k_0 + C^2 k\,(1-i\lambda)\right)\left(\frac{A_0+A_1}{2}\right) - k_0\left(C^2 k(1-i\lambda)\right) A_0 A_1$$

$A_0 = a_0 + ib_0$, $A_1 = a_1 + ib_1$ = the complex scattering lengths for the isotopic-spin 0 and 1 channels respectively,

k_0 = the wave number (center-of-mass system) of the $\bar{K}^0 N$ channel (taken as $i\left|k_0\right|$ below $\bar{K}^0 N$ threshold),

k = the center-of-mass wave number of the $K^- p$ channel,

C^2 = the Coulomb penetration factor $= \frac{2\pi}{kB}\left(1-\exp\left[-2\pi/kB\right]\right)^{-1}$

B = the Bohr radius of the K^--p system

λ = a function of k given by the authors' Eq. (4.12),[14] and

σ_0 and σ_1 = the absorption cross sections in the I=0, I=1 channels respectively.

The following remarks will aid in understanding the various terms of Eqs. (3.1) through (3.4). In the absence of Coulomb effects and the $\bar{K}^0$-n—K^--p mass difference, the elastic cross section for a pure isotopic spin state I is given by

$$\sigma_{el} = 4\pi \left|\frac{A_I}{1-ikA_I}\right| \tag{3.5}$$

where k is the wave number (c.m.) and $A_I = a_I + ib_I$ is the complex scattering length for the channel. A_I is related to the complex phase shift δ_I of scattering theory by the relation

$$k \cot \delta_I = \frac{1}{A_I}\,. \tag{3.6}$$

The zero-effective-range approximation consists of neglecting higher powers in k in the expansion of $k \cot \delta$. The choice of sign in Eq. (3.6) defines A_I in such a way that attractive force in Channel I corresponds to a positive real part of $A_I (a_I > 0)$. The imaginary part of $A_I (b_I)$ is

always positive, corresponding to absorption from the incident beam. In this simplified picture, the absorption cross section is given by

$$\sigma_I = \frac{4\pi b_I}{k} \left| \frac{1}{1-ikA_I} \right|^2 . \tag{3.7}$$

That the K^--p channel consists of both I=0 and I=1 in equal amounts leads to an amplitude for scattering which is one-half the sum of two amplitudes:

$$\sigma_{el} \left[K^- p = \frac{1}{\sqrt{2}} \left(| I = 0 > + | I = 1 > \right) \right] = \pi \left| \frac{\frac{1}{2} A_0}{1-ikA_0} + \frac{\frac{1}{2} A_1}{1-ikA_1} \right|^2 . \tag{3.8}$$

The effect of the $\overline{K}^0$-n—K^--p mass difference is to couple the two I-spin states by kinematical factors in an inseparable way. If k and k_0 are the c.m. wave numbers of the K^--p and $\overline{K}^0$-n channels respectively, then the mass difference effect can be represented by the following transformations on the denominators of Eq. (3.8):

$$\left.\begin{aligned} \frac{1}{1-ikA_0} &\longrightarrow \frac{1-ik_0A_1}{1-i(k_0+k)\left(\frac{A_0+A_1}{2}\right) - k_0k\, A_0A_1} \\ &\text{and} \\ \frac{1}{1-ikA_1} &\longrightarrow \frac{1-ik_0A_0}{1-i(k_0+k)\left(\frac{A_0+A_1}{2}\right) - k_0k\, A_0A_1} \end{aligned}\right\} \tag{3.9}$$

In the limit $k_0 = k$ the denominators in (3.9) reduce to $(1-ikA_0)\cdot(1-ikA_1)$, and the transformation is unity, as it should be. This same transformation, when applied to the charge-exchange amplitude (which is one-half the difference of the I=0 and I=1 amplitudes), and the absorption given by Eq. (3.7), yield the correct Eqs. (3.2) through (3.4), except for the factor C^2 and the definition of the denominator D.

The remaining complication is due to the Coulomb force in the initial state, whose net effect can be described by two changes:

(a) The Coulomb penetration factor C^2 must be used as a multiplicative factor on each scattering amplitude once for each time the K^-p state enters, and

(b) The kinematical factor k occurring in the denominators in Eq. (3.9) must be modified by the transformation

$$k \longrightarrow k C^2 (1 - i\lambda). \tag{3.10}$$

The derivation of these effects is given in Ref. 14, and this prescription is given here only as an aid in understanding the terms entering into Eqs. (3.1) through (3.4). Beside the four real parameters contained in A_0 and A_1, two more parameters are necessary to express the observed hyperon cross sections. We chose these parameters as the ratio γ of $\Sigma^- \pi^+$ to $\Sigma^+ \pi^-$ production at rest, and the ratio ϵ of the $\Lambda \pi^0$ production rate to the total hyperon production rate in the isotopic spin-1 channel at rest. In our analysis we have assumed the following conditions to hold for the parameters of the theory:

(a) The scattering lengths A_0 and A_1 are independent of momentum,

(b) The parameter ϵ is independent of momentum, and

(c) The momentum dependence of the difference in phase angle, $\phi = \phi_0 - \phi_1$, between the matrix elements for $\Sigma\pi$ production in $I=1$ and $I=0$, is given by

$$\phi = \phi_{th} + \arg \frac{1 - ik_0 A_1}{1 - ik_0 A_0} ,$$

where ϕ_{th} = the value of the phase angle at the $\bar{K}^0 N$ threshold (89 Mev/c incident K^- lab momentum).

Condition (c) is used to relate γ to the value of ϕ_{th}, and therefore γ is the parameter that determines the phase ϕ.

The assumption that the capture of K^- on protons at rest takes place with the K^--p system in a relative s state[15] allows the use of the at-rest ratios of the hyperon production rates that are so important in determining the values of the parameters. In terms of $\phi, \epsilon, \sigma_0(A_0, A_1)$, and $\sigma_1(A_0, A_1)$, the hyperon cross sections are given by

$$\sigma(K^- + p \longrightarrow \Sigma^- + \pi^+) = \frac{1}{6}\sigma_0 + \frac{1}{4}(1-\epsilon)\sigma_1 + \frac{1}{\sqrt{6}}\sqrt{\sigma_0\sigma_1(1-\epsilon)}\cos\phi, \tag{3.11}$$

$$\sigma(K^- + p \longrightarrow \Sigma^+ + \pi^-) = \frac{1}{6}\sigma_0 + \frac{1}{4}(1-\epsilon)\sigma_1 - \frac{1}{\sqrt{6}}\sqrt{\sigma_0\sigma_1(1-\epsilon)}\cos\phi, \tag{3.12}$$

$$\sigma(K^- + p \longrightarrow \Sigma^0 + \pi^0) = \frac{1}{6}\sigma_0, \tag{3.13}$$

and

$$\sigma(K^- + p \longrightarrow \Lambda + \pi^0) = \frac{1}{2}\sigma_1\epsilon, \tag{3.14}$$

where σ_1 and σ_0 are given by Eqs. (3.3) and (3.4). In addition, the at-rest ratios are

$$\left.\frac{\Gamma(K^- + p \longrightarrow \Lambda + \pi^0)}{\Gamma(K^- + p \longrightarrow \Lambda + \pi^0) + \Gamma(K^- + p \longrightarrow \Sigma^0 + \pi^0)}\right|_{\text{at-rest}} = \frac{\epsilon b_1 |1 + \kappa A_0|^2}{\epsilon b_1 |1 + \kappa A_0|^2 + \frac{1}{3} b_0 |1 + \kappa A_1|^2}, \tag{3.15}$$

$$\left.\frac{\Gamma(K^- + p \longrightarrow \Sigma^- + \pi^+)}{\Gamma(K^- + p \longrightarrow \Sigma^+ + \pi^-}\right|_{\text{at-rest}} =$$

$$\frac{\frac{b_0}{6}|1 + \kappa A_1|^2 + \frac{(1-\epsilon)b_1}{4}|1 + \kappa A_0|^2 + \frac{1}{\sqrt{6}}\left[|1 + \kappa A_0|^2 \cdot |1 + \kappa A_1|^2 (1-\epsilon)\right]^{1/2}\cos\phi}{\frac{b_0}{6}|1 + \kappa A_1|^2 + \frac{(1-\epsilon)b_1}{4}|1 + \kappa A_0|^2 - \frac{1}{\sqrt{6}}\left[|1 + \kappa A_0|^2 \cdot |1 + \kappa A_1|^2 (1-\epsilon)\right]^{1/2}\cos\phi}, \tag{3.16}$$

and

$$\left.\frac{\Gamma(K^-+p \longrightarrow \Sigma^-+\pi^+)+\Gamma(K^-+p \longrightarrow \Sigma^++\pi^-)}{\Gamma(K^-+p \longrightarrow \Sigma^0+\pi^0)+\Gamma(K^-+p \longrightarrow \Lambda+\pi^0)}\right|_{\text{at-rest}} = \frac{\frac{b_0}{3}\left|1+\kappa A_1\right|^2+\frac{(1-\epsilon)b_1}{2}\left|1+\kappa A_0\right|^2}{\frac{b_0}{6}\left|1+\kappa A_1\right|^2+\frac{\epsilon b_1}{2}\left|1+\kappa A_0\right|^2}, \tag{3.17}$$

where κ is the absolute value of the wave number in the $\bar{K}^0$-N channel for zero K^--p relative momentum (i.e., $\kappa = \left|k_0(P_{K^-} = 0)\right|$).

Many pieces of experimental data are available for the determination of the parameters and, for the purpose of describing them, they are represented by $\sigma_{aj}{}^m$ where m stands for "measured." Symbol a varies from 1 to 12, depending on the physical process for which a measurement has been made, and j varies with the lab momentum of the K^- for which the measurement was made. A zero value for j means a measurement at rest; j=1 corresponds to the momentum interval $0 \leqslant P_{klab} \leqslant 25$ Mev/c, and so on for 25-Mev/c intervals. In Table IV we indicate what measurements have contributed to the determination of the parameters.

A value corresponding to each measurement was calculated from the theory by assuming values for the parameters. We then calculated a χ^2 for the experiment from the equation

$$\chi^2(A_0, A_1, \gamma, \epsilon) = \sum_{a=1}^{12} \sum_{j=a_a}^{b_a} \sum_{k=a_a}^{b_a} (\sigma_{aj}-\sigma_{aj}{}^m)\,(E^a)_{jk}{}^{-1}(\sigma_{ak}-\sigma_{ak}{}^m), \tag{3.18}$$

where E^a is the variance-covariance matrix for measurements in the class a. A minimum in the χ^2 was sought by the following simple procedure. A central value for the six parameters was chosen and χ^2 calculated. The χ^2 space was investigated in the neighborhood of this point by displacing each parameter in turn by a small amount on either side of its central value and calculating the corresponding value of χ^2. Holding all but one variable fixed, and assuming χ^2 to be a quadratic function of the variable under consideration, we calculated the expected change in χ^2 and the step necessary to make it. The calculation was

Table IV

Physical measurements contributing to the determination of the s-wave zero-effective-range parameters

α	Physical quantity measured $\sigma^m_{\alpha j}$	$a_\alpha \leq j \leq b_\alpha$		No. of msrmts	Total range of K^-lab momentum (Mev/c)
		a_α	b_α		
1	$\int_{-1.00}^{0.85} \frac{d\sigma_{el}}{d\Omega} d\Omega$	5	11	7	100-275
2	$\int_{0.85}^{0.90} \frac{d\sigma_{el}}{d\Omega} d\Omega$	5	11	7	100-275
3	$\int_{0.90}^{0.95} \frac{d\sigma_{el}}{d\Omega} d\Omega$	5	11	7	100-275
4	$\int_{0.95}^{0.966} \frac{d\sigma_{el}}{d\Omega} d\Omega$	5	11	7	100-275
5	$\sigma(K^- + p \to \bar{K}^0 + n)$	5	11	7	100-275
6	$\sigma(K^- + p \to \Sigma^- + \pi^+)$	3	11	9	50-275
7	$\sigma(K^- + p \to \Sigma^+ + \pi^-)$	4	11	8	75-275
8	$\sigma(K^- + p \to \Sigma^0 + \pi^0) + \sigma(K^- + p \to \Lambda + \pi^0)$	6	10	5	125-250
9	$\frac{\sigma(K^- + p \to \Lambda + \pi^0)}{\sigma(K^- + p \to \Lambda + \pi^0) + \sigma(K^- + p \to \Sigma^0 + \pi^0)}$	7	10	4	150-250
10	$\frac{\Gamma(K^- + p \to \Lambda + \pi^0)}{\Gamma(K^- + p \to \Lambda + \pi^0) + \Gamma(K^- + p \to \Sigma^0 + \pi^0)}$	0	0	1	At rest
11	$\frac{\Gamma(K^- + p \to \Sigma^- + \pi^+)}{\Gamma(K^- + p \to \Sigma^+ + \pi^-)}$	0	0	1	At rest
12	$\frac{\Gamma(K^- + p \to \Sigma^- + \pi^+) + \Gamma(K^- + p \to \Sigma^+ + \pi^-)}{\Gamma(K^- + p \to \Sigma^0 + \pi^0) + \Gamma(K^- + p \to \Lambda + \pi^0)}$	0	0	1	At rest
				64 Total	

made for each variable and a step was taken by changing only that variable for which the largest change in χ^2 was predicted. Although this is probably not the most efficient method, it always led to a lower value of χ^2. The χ^2 space was again investigated in the neighborhood of the new central values and another step taken. The procedure was repeated until no step could be taken that would improve the value of χ^2.

The starting values of the parameters A_0 and A_1 were taken to be the values recently calculated by Dalitz.[16] He has calculated four sets of solutions based on preliminary reports of our data on elastic and charge-exchange scattering, and absorption yielding charged Σ at 172 Mev/c, together with the at-rest ratios of hyperon production. A phase-shift analysis of the K^--p data at a given momentum with neglect of the $\bar{K}^0 n - K^- p$ mass difference and Coulomb effects in the initial channel leads to a four-fold-degenerate set of solutions. A brief analysis of this type has been given by Kruse and Nauenberg.[17] That Dalitz calculates four solutions is intimately related to this basic degeneracy. Two of the solutions have a positive real part for the scattering lengths. The other two have negative real parts. Hence half the degeneracy should be resolved by investigating the Coulomb nuclear interference. However, since the scattering is dominated by absorption, the amplitude is mainly imaginary, and the difference between positive and negative interference is much less than it would be for a system with no absorption. The other half of the degeneracy is related to the fact that there are two I-spin channels involved, and only the phase of the sum of the individual amplitudes is measured. The absorption in the individual I-spin channels allows a determination of the magnitude of $e^{2i\delta_I} = \eta_I e^{2i\alpha_I}$ through the relation

$$\sigma_I = \frac{\pi}{k^2} (1 - \eta_I^2). \tag{3.19}$$

The charge-exchange scattering then determines the magnitude of the phase difference $\Delta_a = \pm 2 \left| a_0 - a_1 \right|$, and by the simple geometrical construction according to Kruse and Nauenberg[17] this leads to the magnitude of the sum of these phases. The choice of sign for the phase difference Δ_a constitutes the remaining degeneracy.

Data used in Dalitz's calculations[16] did not contain information on the variation of cross sections with momentum or the Coulomb nuclear interference. It is reasonable to expect the above-mentioned degeneracy to be broken by sufficient information on the momentum dependence of the cross sections and the Coulomb nuclear interference. Indeed, we find only two distinct minima in the χ^2 function, and one of these is a considerably better fit to the data than the other. The values of the parameters giving minima in the χ^2 function and the values of χ^2 at these minima are given in Table **V**. Table VI gives a breakdown of the contribution to the total χ^2 from the different physical processes (a) defined in Table IV. The uncertainties in the parameters were estimated by using second differences to calculate the second-derivative matrix of the χ^2 function at the two minima. Two times the inverse of this matrix gives the variance-covariance matrix for the parameters. Tables VII and VIII contain these matrices for Solutions 1 and 2 respectively. The square root of the diagonal terms are the uncertainties quoted in Table V.

We also include the second-derivative matrix in Tables VII and VIII for the purpose of describing the χ^2 space. The χ^2 function is given by

$$\chi^2 = (\underline{\beta} - \underline{\beta}^*) \cdot \underset{\sim}{D} \cdot (\beta - \beta^*) \tag{3.20}$$

in the neighborhood of the solutions β^* of Table V. The components of β in terms of the parameters are given by:

Table V

Values of the s-wave zero-effective-range parameters, giving minima in the χ^2 function

Solution	$A_0(f)$		$A_1(f)$		$\gamma(\phi_{th})$	ϵ	χ^2 58 deg. of freedom	$P(\chi^2)$ (%)
	a_0	b_0	a_1	b_1				
1	-0.22 ±1.07	2.74 ±0.31	0.02 ±0.33	0.38 ±0.08	2.15 ±0.16(96)	0.40 ±0.03	57.91	48
2	-0.59 ±0.46	0.96 ±0.17	1.20 ±0.06	0.56 ±0.15	2.04 ±0.18(-50)	0.39 ±0.02	73.49	8

Table VI

Contributions of the different physical measurements to the final value of χ^2 for solutions 1 and 2 of Table V

a	Number of measurements	Solution 1 χ^2	Solution 2 χ^2
1	7	7.56	15.21
2	7	2.66	3.73
3	7	1.79	1.91
4	7	3.93	3.49
5	7	2.14	2.20
6	9	9.31	11.80
7	8	10.76	7.21
8	5	13.19	15.39
9	4	6.28	9.28
10	1	0.27	2.27
11	1	0.00	0.88
12	1	0.02	0.11
Total	64	57.91	73.49

Table VII

Variance-covariance matrix (top) and second derivative matrix D (bottom) for the parameters of Solution 1, Table V

$$\left[\chi^2 = (\underline{\beta}-\underline{\beta}^*) \cdot \underset{\sim}{D} \cdot (\underline{\beta}-\underline{\beta}^*)\right]$$

Label	Variance-covariance					
	a_0	b_0	a_1	b_1	γ	ϵ
$\beta_1=a_0$	1.15	1.22×10^{-1}	0.28	-0.51×10^{-1}	-0.52×10^{-2}	-0.98×10^{-2}
$\beta_2=b_0$	1.22×10^{-1}	0.99×10^{-1}	0.33×10^{-1}	-0.92×10^{-2}	0.74×10^{-2}	0.32×10^{-3}
$\beta_3=a_1$	0.28	0.33×10^{-1}	1.08×10^{-1}	-0.90×10^{-2}	-1.12×10^{-2}	-1.23×10^{-3}
$\beta_4=b_1$	-0.51×10^{-1}	-0.92×10^{-2}	-0.90×10^{-2}	0.56×10^{-2}	-0.65×10^{-3}	-1.55×10^{-4}
$\beta_5=\gamma$	-0.52×10^{-1}	0.74×10^{-2}	-1.12×10^{-2}	-0.65×10^{-3}	0.27×10^{-1}	-0.28×10^{-3}
$\beta_6=\epsilon$	-0.98×10^{-2}	0.32×10^{-3}	-1.23×10^{-3}	-1.55×10^{-4}	-0.28×10^{-3}	0.72×10^{-3}
	Second derivative(D)					
a_0	1.21×10	-9.48×10^{-2}	-2.42×10	7.48×10	-4.45	1.37×10^{2}
b_0	-9.48×10^{-2}	2.59×10	-6.24	2.99×10	-9.26	-2.08×10
a_1	-2.42×10	-6.24	7.37×10	-1.17×10^{2}	2.26×10	-2.15×10^{2}
b_1	7.48×10	2.99×10	-1.17×10^{2}	9.26×10^{2}	-9.13	9.92×10^{2}
γ	-4.45	-9.26	2.26×10	-9.13	8.58×10	1.46×10
ϵ	1.37×10^{2}	-2.08×10	-2.15×10^{2}	9.92×10^{2}	1.46×10	4.47×10^{3}

Table VIII

Variance-covariance matrix (top) and second derivative matrix D (bottom) for the parameters of Solution 2, Table V

$$\left[\chi^2 = (\underline{\beta}-\underline{\beta}^*) \cdot \underset{\sim}{D} \cdot (\underline{\beta}-\underline{\beta}^*)\right]$$

Label	a_0	b_0	a_1	b_1	γ	ϵ
			Variance-covariance			
$\beta_1=a_0$	0.21	1.26×10^{-1}	-1.07×10^{-1}	-0.51×10^{-1}	-0.43×10^{-1}	-0.49×10^{-3}
$\beta_2=b_0$	1.26×10^{-1}	0.28×10^{-1}	-0.53×10^{-2}	-0.38×10^{-1}	-0.28×10^{-2}	-0.32×10^{-3}
$\beta_3=a_1$	-1.07×10^{-1}	-0.53×10^{-2}	0.36×10^{-2}	0.37×10^{-1}	-0.41×10^{-2}	0.73×10^{-3}
$\beta_4=b_1$	-0.51×10^{-1}	-0.38×10^{-1}	0.37×10^{-1}	0.22×10^{-1}	1.18×10^{-2}	-0.92×10^{-3}
$\beta_5=\gamma$	-0.43×10^{-1}	-0.28×10^{-2}	-0.41×10^{-2}	1.18×10^{-2}	0.33×10^{-1}	0.61×10^{-3}
$\beta_6=\epsilon$	-0.49×10^{-3}	-0.32×10^{-3}	0.73×10^{-3}	-0.92×10^{-3}	0.61×10^{-3}	0.54×10^{-3}
			Second derivative (D)			
a_0	4.15×10	-4.07×10	-4.23×10	1.12×10^2	0.583	2.59×10^2
b_0	-4.07×10	1.39×10^2	1.29×10^2	-1.01×10^2	1.66×10	-3.17×10^2
a_1	-4.23×10	1.29×10^2	1.02×10^2	-5.58×10	-7.93	-1.84×10^2
b_1	1.12×10^2	-1.01×10^2	-5.58×10	3.00×10^2	1.16×10	6.10×10^2
γ	0.583	1.66×10	-7.93	1.16×10	5.75×10	-2.43×10
ϵ	2.59×10^2	-3.17×10^2	-1.84×10^2	6.10×10^2	-2.43×10	5.02×10^3

$$\beta_1 = a_0$$
$$\beta_2 = b_0$$
$$\beta_3 = a_1$$
$$\beta_4 = b_1$$
$$\beta_5 = \gamma$$
$$\beta_6 = \epsilon \ .$$

If independent information is available on some of the parameters β, then the best way to change the other parameters to accept this new information is dictated by the shape of the χ^2 space given by Eq. (3.20).

Curves of the elastic-scattering cross section and the change-exchange cross section corresponding to Solution 1 are given in Figs. 7 and 10 respectively.

B. Coulomb Nuclear Interference

The s-wave zero-effective-range analysis above does contain information on the Coulomb nuclear interference, but the inclusion of all other information partially obscures its part in the final solution. For this reason, it was considered desirable to analyze the Coulomb nuclear interference separately, independent of any assumptions on the momentum dependence or isotopic-spin dependence of the cross section. To this end, we write the differential scattering cross section for K^--p elastic scattering in the form

$$\frac{d\sigma_{el}}{d\Omega} = \left| \frac{\csc^2(\theta/2)}{2Bk^2} \exp\left[i \frac{2}{kB} \ln \sin \frac{\theta}{2} \right] + C^2 R \exp\left[i\alpha \right] \right|^2 \tag{3.21}$$

The first term on the right is the Coulomb part of the scattering amplitude, k is the center-of-mass wave number, and B is the Bohr radius of the K^--p system. The second term represents the s-wave nuclear amplitude (modified by C^2, the real s-wave Coulomb penetration factor); hence, $R \cos \alpha$ and $R \sin \alpha$ are the real and imaginary parts of the nuclear amplitude. The Coulomb amplitude is dominant at small angles, but decreases rapidly with increasing angle.

At some angle θ_c the Coulomb amplitude will be equal in magnitude to the nuclear amplitude, and at this point the differential-scattering cross section can vary from 0 to 4 C^4R^2, depending on the value of α. At larger angles, the cross section will be dominated by the term C^4R^2. Because of this interference between the two amplitudes, we have been able to estimate the values of R and α for the two measurements of the K^--p elastic differential-scattering cross section shown in Fig. 6. The method used was similar to the minimization of $\chi^2(A_0, A_1, \gamma, \epsilon)$ as discussed in Sec. IV-A, except that in this case we could make a contour map of the χ^2 function, since χ^2 is a function of only the two parameters (R, α). In Table IX we give the values of R and α that minimize the χ^2 function for the two momentum intervals. The uncertainties were obtained from the contour on which the value of χ^2 differed by 1 from its minimum value.

The small real part of the nuclear amplitude indicated by these values of R and α is in agreement with the large values observed for the total absorption cross sections, and is another manifestation that the low-momentum K^--p interactions are dominated by very strong absorption processes. The average values of the phase of the nuclear amplitude for the two s-wave zero-effective-range solutions of Sec. IV-A are given in Table X for comparison.

Table IX

Values of the modulus and phase of the nuclear part of the elastic-scattering amplitude as determined from the elastic-differential-scattering cross sections in Fig. 6

K^- lab momentum Interval (Mev/c)	R (fermis)	α (deg)	Rα Correlation	C^2
100-175	0.81±0.06	78±31	+0.84	1.085
175-250	0.62±0.04	97±38	+0.78	1.058

Table X

Average phase of the nuclear amplitude calculated from the s-wave zero-effective-range parameters of Solutions 1 and 2, and the phase obtained from the differential-scattering cross sections of Fig. 6

Solution	α (deg) (100 Mev/c-175 Mev/c)	α (deg) (175 Mev/c-250 Mev/c)
1	91	90
2	75	78
Experimental (Table IX)	78±31	97±38

V. CONCLUSIONS

The absorption channels open to the low-energy K^--p system are so strong that they dominate the elastic scattering. The strong damping introduced by these absorptions changes what we would expect to be a constant elastic cross section to one resembling the $1/v$ law expected of an absorption cross section. The elastic nuclear-scattering amplitude is nearly pure imaginary and, therefore, interferes very little with the Coulomb amplitude, which is nearly real.

A simple s-wave zero-effective-range parameterization is adequate to describe the K^--p interaction within the limits of the present data. More data will undoubtedly call for modifications in the theory. The scattering lengths A_0 and A_1 may vary with momentum, the assumption of zero effective range may need to be lifted, and the whole analysis will have to be joined at the higher momenta with a p-wave theory. At least ten times as much data as presently available will be necessary to separate the effects of, say, variation of A_0 and A_1 with momentum and the effects of the addition of a nonzero range for all the channels. We now have three times as much K^--p data on film as reported on here, and these data are in the process of being analyzed.

ACKNOWLEDGMENTS

The investigation of elementary particle interactions with tools such as the Berkeley Bevatron, the 15-inch hydrogen bubble chamber, and high-speed digital computers necessarily involves the effort of many people. It is with pleasure that I acknowledge the aid and support of Professor Luis Alvarez and the guidance of Professor Arthur H. Rosenfeld. Many thanks are due Dr. Nahmin Horwitz, Dr. Joseph Murray, and Dr. Robert Tripp, with whom I worked during the construction and operation of the beam. I am indebted to Dr. Frank Solmitz for his advice and teaching in the fields of data analysis and statistics.

I express my gratitude to Dr. William Humphrey, Dr. Paul Nordin, Jr., and Mr. Peter Berge for their help in this collaborative effort of data analysis.

Thanks are due to many scanners and technicians, in particular to Mr. Jim Neufeld and Mrs. Karen Profet.

I am grateful for the experimental facilities provided by the Bevatron staff, for the efforts of the bubble-chamber operating crew headed by Messrs. Glenn Eckman and Robert Watt, and for the co-operation of the campus staff of computer operators.

Finally, I thank my wife, Lee, for her encouragement and understanding during the period of this work.

This work was done under the auspices of the U. S. Atomic Energy Commission.

APPENDICES

A. The Use of Experimental Distributions of χ^2 and the "Stretch" Quantities S_i to Study the Uncertainties in the Observed Variables

The quantity χ^2 is a well-known test function generally used to test the consistency of an hypothesis with a given set of experimental data.[18] In our case there is no question regarding the hypothesis for elastic scattering because of the characteristic appearance of the events in the bubble chamber and the relatively low incident momentum. Hence we can use the χ^2 test function to study the consistency of the measurements and their uncertainties. From the theory of statistics, the frequency function of χ^2, $P_n(\chi^2)$, is given by

$$P_n(\chi^2) = \frac{1}{2^{n/2}\Gamma(n/2)} (\chi^2)^{(n/2)-1} \exp\left[-\chi^2/2\right] , \qquad \text{(A-1)}$$

where n is the number of degrees of freedom of χ^2 and is discussed below. The properties of $\Gamma(x)$ useful for evaluation of Eq. (A-1) are:

$$\Gamma(x+1) = x\,\Gamma(x) ,$$

and

$$\Gamma(1/2) = \sqrt{\pi} ,$$

$$\Gamma(1) = 1.$$

We compare the observed distribution of values of χ^2 for many events with the theoretical distribution given by (A-1). Deviations from the theoretical distributions can arise from improper assignment of uncertainties to the measured variables, systematic errors in measurement, or the breakdown of certain assumptions made in the kinematical analysis (such as the assumption of normally distributed variables, or the "local linearity" of the constraint equations).

The number of degrees of freedom n of the χ^2 distribution function in Eq. (A-1) is given by

$$n = M - P, \qquad \text{(A-2)}$$

where M is the number of independent measurements and P is the

number of independent parameters in the hypothesis being tested. For N particles interacting at a vertex (counting initial and final states), the number of independent parameters is given by

$$P = 3N-4, \tag{A-3}$$

as follows from the fact that once the values of 3N-4 variables are known, the four remaining variables can be calculated from the four equations of momentum and energy conservation. The number of measurements can vary from 0 to 3N, but the only cases for which a χ^2 can be calculated are 3N, 3N-1, 3N-2, and 3N-3, corresponding respectively to 0, 1, 2, and 3 variables not measured. Using Eqs. (A-2) and (A-3), we find the values of n for these cases are 4, 3, 2, and 1 (note that in each case n is equal to the number of constraining equations left after the missing variables have been calculated). For the majority of the elastic scatterings (279) all variables were measured, and therefore the χ^2 for these events had four degrees of freedom. This group of highly overdetermined elastic scatterings was used to study the measurements and their uncertainties.

In Fig. 11 we have plotted a histogram of the number of events as a function of χ^2. Curve A of the figure is a graph of the function $P_4(\chi^2)$ normalized to the 279 events. Clearly, the experimental distribution is more "spread out" than the theory predicts. The mean of the observed distribution is 5.86, as compared with 4 for the theoretical curve. Curve B is a graph of a function $\left[Q_4(\chi^2)\right]$ having the same mean as the experimental distribution and derived from the function $P_4(\chi^2)$ by assuming a 21% underestimate of the uncertainties in all measured variables. $Q_4(\chi^2)$ is given by

$$Q_4(\chi^2) = \frac{279}{(1.21)^2} P_4 \left(\frac{\chi^2}{(1.21)^2}\right) . \tag{A-4}$$

The agreement between Curve B and the observed distribution suggests that the major cause of the discrepancy between the observed distribution and theory is due to underestimated uncertainties in the measured variables.

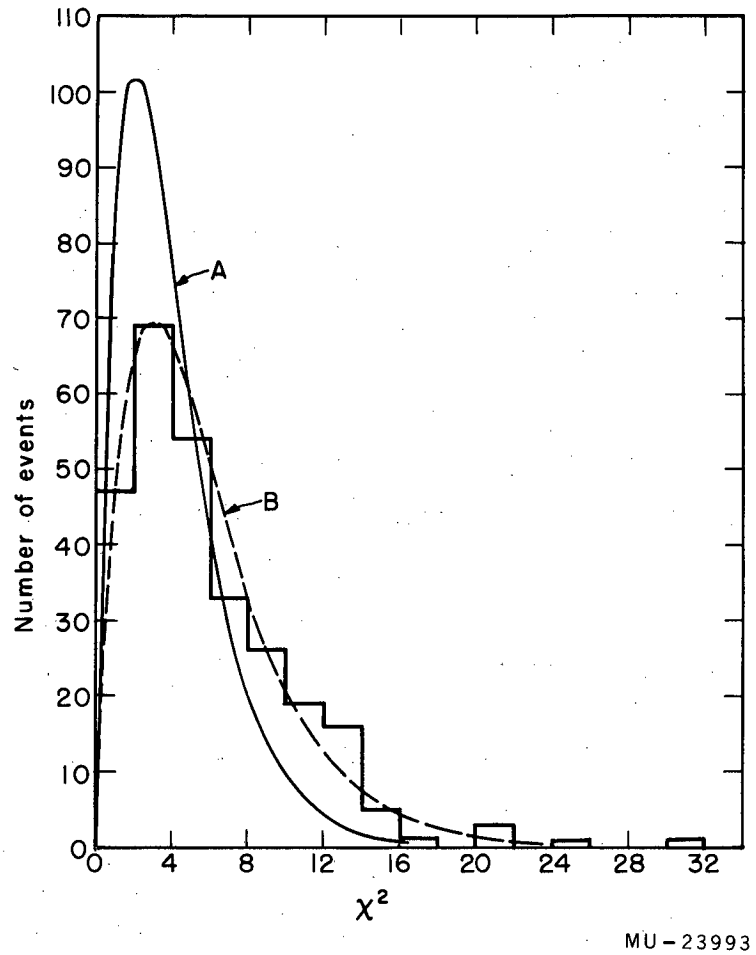

Fig. 11. Distribution of χ^2 for 279 4c elastic scatterings. Curve A is the theoretical frequency function for four degrees of freedom (Eq. A.1). Curve B is the theoretical frequency function appropriate to a 21% underestimate of uncertainties of the measured values (Eq. A.4).

To determine the contribution of individual variables to the observed discrepancy, we make use of the test quantities $S_i(x)$, which are called the "stretch" of the variable x and are defined by the equation

$$S_i(x^*) = \frac{x_i^* - x_i^m}{(x_i^* - x_i^m)_{rms}}, \qquad \text{(A-5)}$$

where x_i^* is the final adjusted value of the variable corresponding to the measured variable x_i^m. The quantity $(x_i^* - x_i^m)_{rms}$ is calculated at the time of the fit and is an estimate of the width of the distribution of x_i^* about x_i^m for this particular event. The $(x_i^* - x_i^m)_{rms}$ is <u>not</u> the same as the width of the distribution of x_i^m about the true value of x_i [a complete discussion of the quantity $(x_i^* - x_i^m)_{rms}$, as well as of $S_i(x)$ and other equations relevant to the kinematical fitting done in KICK, has been given by Berge, Solmitz, and Taft[19]]. The distribution of the S_i should have a mean value 0 if there are no systematic effects, and a standard deviation 1 if the uncertainties used to calculate $(x_i^* - x_i^m)_{rms}$ are correct. The variables x_i used in KICK to specify a track, and so those for which the quantities S_i are calculated, are the following:

ϕ_q = the azimuthal angle of the <u>q</u>th particle,

$\tan\lambda_q$ = the tangent of the latitude of the <u>q</u>th particle,

and

k_q = the "projected curvature" of the <u>q</u>th particle, defined by

$$k_q = \left[P_q \cos \lambda_q\right]^{-1},$$

where P_q is the momentum in Mev/c of the <u>q</u>th particle.

The distribution of $S_i(x)$ for these variables (for the 279 4C elastic-scattering events) is shown in Figs. 12 to 14. Figure 12 contains the distributions of $S(\phi)$, $S(\tan\lambda)$, and $S(k)$ for the incident K^- meson; Fig. 13, those for the scattered K^-; and Fig. 14, those for the recoil proton. The solid curve on each figure is a normal distribution with a standard deviation equal to the standard deviation of the experimental distribution.

None of the distributions deviates significantly from a normal distribution curve and, hence, within the accuracy of the data, the assumption of normally distributed variables is borne out. In most cases, the mean is consistent with zero, and in all cases it is a small fraction of the corresponding width of the distribution. The value of x_i^2 for a distribution of width w, due to a displacement of the mean from zero by an amount M, is given by

$$x_i^2 = w^2 + M^2 . \qquad \text{(A-6)}$$

Therefore, the observed displacements M_i represent only a small contribution to the observed widening of the χ^2 distribution.[20]

We are led to the conclusion that the main effect on the width of the χ^2 distribution is the width of the S_i distributions. Figure 11(c) shows that the distribution of the pulls of the variable k for the incident K^- track has standard deviation 1. The measurement of this variable is equivalent to a measurement of the sagitta of the track, and — at the momenta considered — its uncertainty is primarily owing to multiple Coulomb scattering. This indicates that the uncertainties in momenta resulting from to multiple Coulomb scattering are correct. The corresponding distributions S(k) for the recoil K^- and proton are wider. In these cases, k is determined by a measurement of the range of the track (which usually comes to rest in the chamber) and so the width of the distribution indicates an underestimate of the uncertainties in length measurement. The widest distributions are those of the variables corresponding to angle measurement. The major factor contributing to these broad widths is the neglect of uncertainties in optical constants, and uncertainties associated with the measurements of fiducial marks.

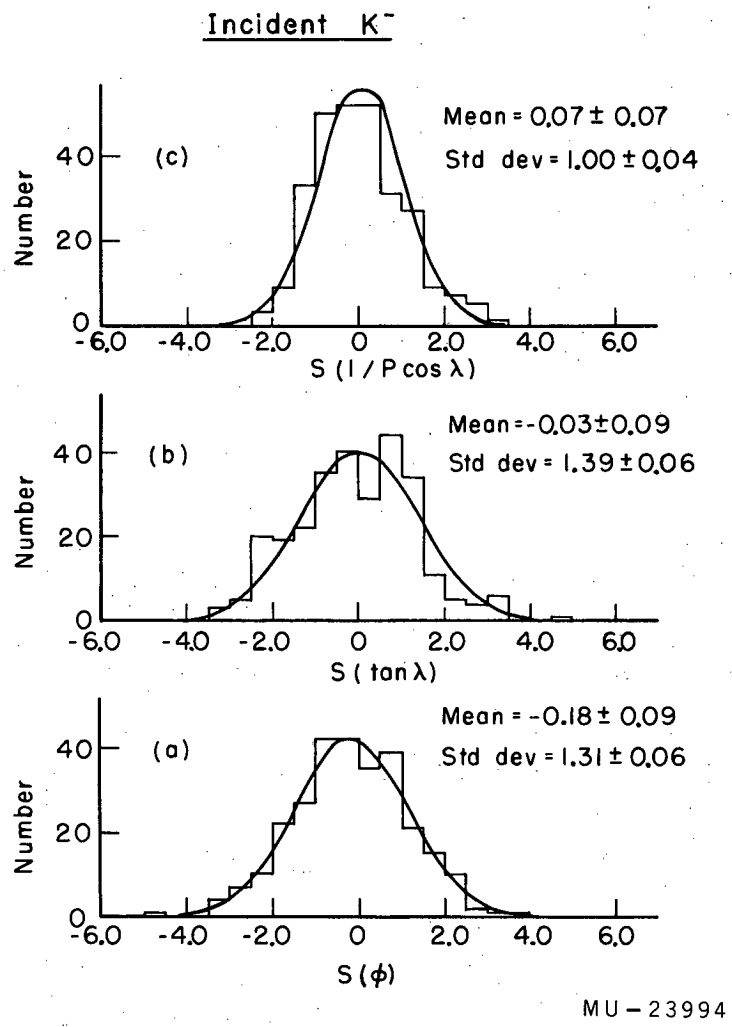

Fig. 12. Distribution of $S_i(x)$ (the "stretch" of x necessary to satisfy the constraints) for the incident K^- tracks of 279 4c elastic scatterings: (a) $x=\phi_{K^-}$, (b) $x=\tan\lambda_{K^-}$, and (c) $x = \frac{1}{P_{K^-}\cos\lambda_{K^-}}$. Curves are frequency functions for a normal distribution with mean and width as indicated.

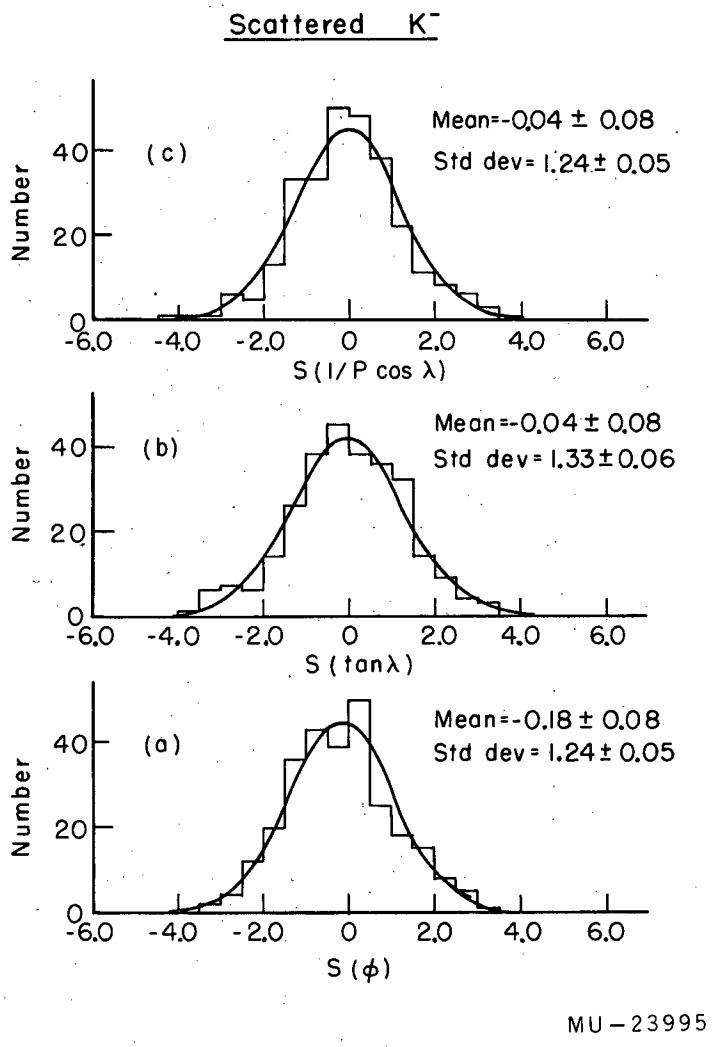

Fig. 13. Distribution of $S_i(x)$ for the scattered K^- tracks of 279 4c elastic scatterings: (a) $x=\phi_{K^-}$, (b) $x=\tan\lambda_{K^-}$, and (c) $x = \frac{1}{P_{K^-}\cos\lambda_{K^-}}$. Curves are frequency functions for a normal distribution with mean and width as indicated.

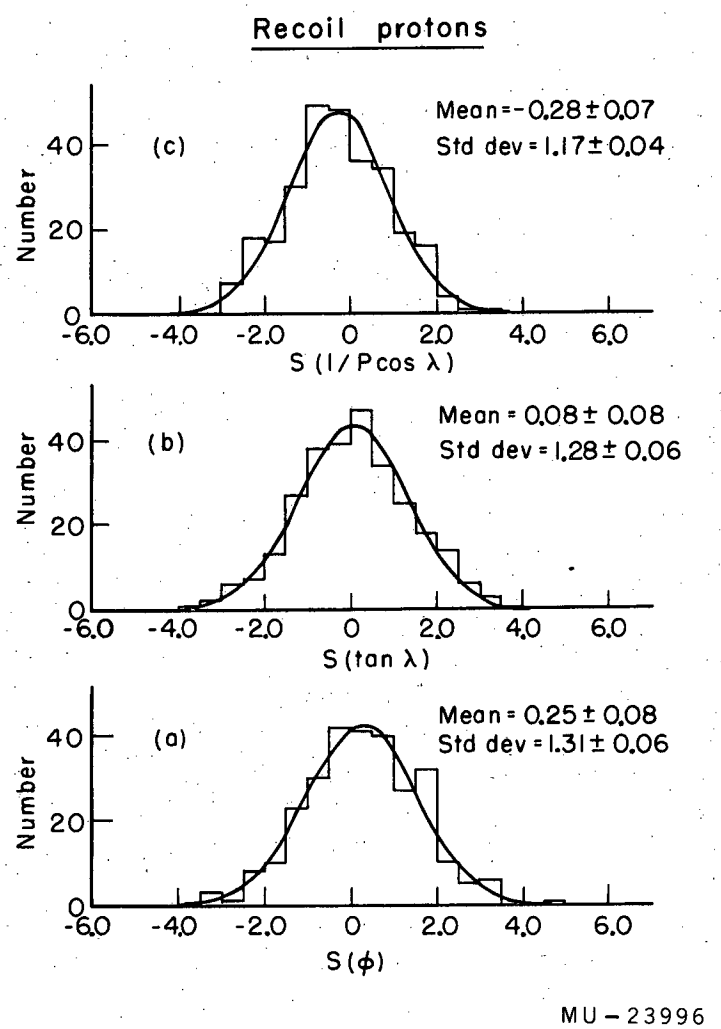

Fig. 14. Distribution of $S_i(x)$ for the recoil-proton tracks of 279 4c elastic scatterings: (a) $x-\phi_p$, (b) $x=\tan\lambda_p$, and (c) $x = \frac{1}{P_p \cos\lambda_p}$. Curves are frequency functions for a normal distribution with mean and width as indicated.

The effect of underestimating these uncertainties on the data of this experiment is found negligible compared with the inherent statistical uncertainties. The information from these distributions will be used to empirically adjust the uncertainties assigned in the program PANG, with the hope that correction of the major effects will allow a study of more subtle difficulties with larger numbers of events.

APPENDIX B

B. The Distribution of Pathlength as a Function of Momentum

Several factors peculiar to this experiment necessitated special care in determining the momentum distribution of the pathlength. First, in order to get sufficient K^- flux, it was necessary to design the beam with a momentum spread of 5% (at 450 Mev/c), which corresponds to a K^- stopping distribution in liquid hydrogen about twice as wide as the 15-inch bubble chamber. Hence, for this low-energy experiment, we were forced to accept a beam in which about half of the K^- stopped in the chamber and the other half went through it. Secondly, the distribution in momentum of the K^- at entrance to the chamber had a steep edge at high momenta (containing mostly those particles that go through the chamber) and a long sloping tail on the low-momentum side. This shape resulted from degrading the symmetric distribution at 450 Mev/c by material in the beam, and is directly attributable to the nonlinear nature of the range-momentum relationship. The problem was further complicated by the fact that there were four different absorber settings during the course of the experiment. In order to avoid introducing any additional sharp discontinuities in the momentum distribution of the K^- tracks at the entrance to the fiducial volume, we analyzed the four groups separately. Finally, the momentum measurement from curvature of the KGT tracks had typical uncertainties of ±10 Mev/c, which meant that there was

considerable smearing of the momentum distribution on the high-momentum side (that is, more tracks were observed with high momentum because of the much larger number of tracks at slightly lower momentum). Because of this smearing, measurements of pathlength as a function of momentum on the individual KGT tracks would introduce serious bias in the pathlength at high momentum. These considerations led us to first estimate the true momentum distribution of the K^- mesons that entered the fiducial volume, and then to predict the amount of pathlength in momentum intervals on the basis of this distribution. The sum of the pathlength in these momentum intervals was constrained to equal the total observed pathlength. The remainder of Appendix B is devoted to a detailed description of the procedure used.

1. "True" Momentum Distribution of K^- Mesons Entering the Fiducial Volume

The particles entering the fiducial volume were divided into three classes: KGT, K^- interactions, and K^- decays. The momentum distribution for each class was determined separately.

In the KGT class, the number of tracks was large enough to give statistically significant numbers in a histogram of the number of tracks per 25-Mev/c interval. Also, the momentum uncertainties of tracks in this class were nearly equal because of the nearly equal lengths of tracks going through the chamber. This combination of good statistics and similar momentum uncertainties for all tracks allowed us to accurately estimate the true distribution by "unfolding" the observed distribution.

The relationship between the observed and the "true" distribution is:

$$D_i = \sum_{j=1}^{N} T_{ij} d_j , \qquad \text{(B-1)}$$

where

D_i = the observed number of events in the ith interval,

d_j = the true number of events in the jth momentum interval,

T_{ij} = the probability that a track with true momentum in the jth interval would have an observed momentum in the ith interval.

The elements of the matrix T_{ij} were calculated to a good approximation by the formula

$$T_{ij} = \frac{1}{\Delta} \int_{P_i - \Delta/2}^{P_i + \Delta/2} dP' \int_{P_j - \Delta/2}^{P_j + \Delta/2} dP \frac{1}{\left[2\pi\sigma_j^2\right]^{1/2}} \exp\left[-\frac{1}{2}\left(\frac{P-P'}{\sigma_j}\right)^2\right]. \qquad \text{(B-2)}$$

The value of Δ in the above expression was 25 Mev/c, and σ_j was set equal to the average uncertainty in momentum of tracks in momentum bin j. The estimate of the true distribution of KGT tracks was then taken as

$$d_j^* = \sum_i (T^{-1})_{ij} D_i . \qquad \text{(B-3)}$$

Figure 15 shows the results obtained for the absorber setting contributing the most pathlength. The solid lines correspond to observed numbers and the d_j^* are represented by dotted lines.

The shape of the momentum distribution of the K^- interactions was established from the data of events having well-determined momenta. Most of these events had momentum uncertainties less than 2.5 Mev/c, although uncertainties as large as 5 Mev/c were accepted. The shape of the distribution of the well-determined events was normalized to the total number of interactions observed.

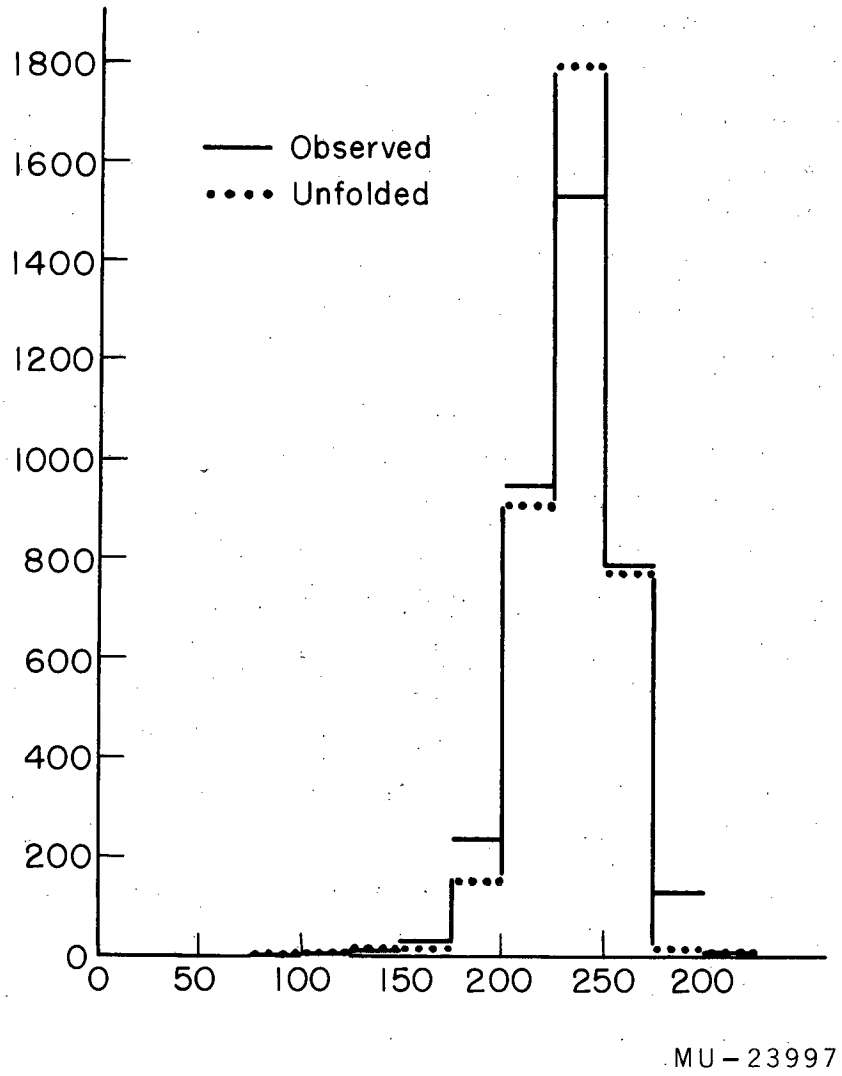

Fig. 15. Number of KGT (K-Go-Through) tracks as a function of the K^- momentum at the entrance to the fiducial volume. Solid lines are the observed numbers, and broken lines represent the estimate of the "true" distribution obtained by unfolding the observed distribution.

The number of K^- decays is about 10% of the total number of K^-. The decays are not kinematically fitted and have shorter K^- tracks than those of the KGT sample. The measurement of these short tracks led to uncertainties in momentum varying from 10 to 30 Mev/c. Because of the poor information available on these tracks, we used our knowledge of the KGT and interactions distributions and established the K-decay distribution by an iterative method. As a first approximation, we took the observed K-decay distribution. Summing of the KGT, K^- interactions, and first-approximation K-decay distributions gave an estimate of the total K^--momentum distribution at entry to the fiducial volume. For each 25-Mev/c momentum interval we then calculated the probabilities of a K^-'s decaying and interacting in cells in the chamber at succeedingly larger distances from the entrance to the fiducial volume. For tracks in a given momentum interval, the decay probability summed over all cells, when multiplied by the number of events in the approximate total distribution, gave a new estimate for the number of K^- in that interval which subsequently decay. The corrected K-decay distribution was then added to the distribution of the KGT's and the interacting K^-'s to form the final estimate of the momentum distribution of K^- tracks entering the fiducial volume. Figure 16 shows the distributions observed (solid lines) together with the final estimates of the true distributions (dotted lines) for the four absorber settings. These estimates of the true distribution were used in the prediction of the pathlength as a function of momentum. This is discussed next.

2. Pathlength as a Function of Momentum

The following idealizations and conventions were adopted in estimating the distribution of pathlength in 25-Mev/c momentum intervals:

(a) The length of all tracks that pass through the fiducial volume is the same; this length (L) is taken as the average length of the tracks in the KGT sample.

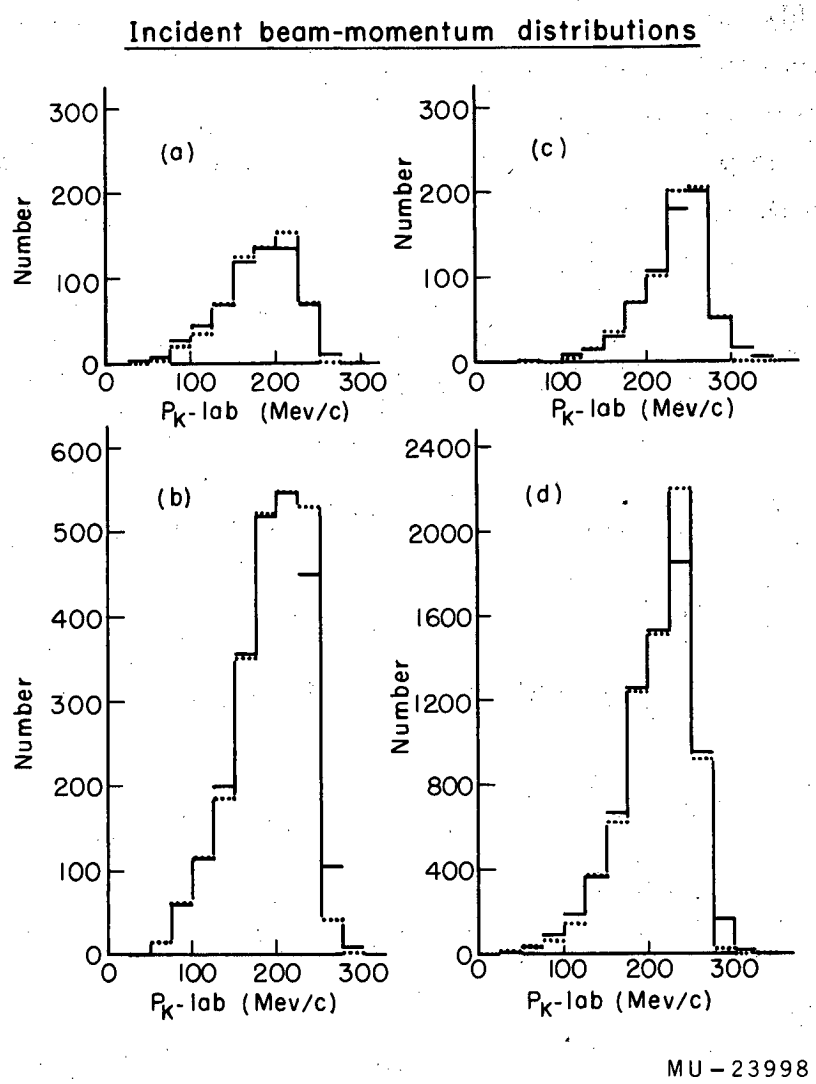

Fig. 16. Momentum distribution of K^- mesons at the entrance to the fiducial volume for the four absorber settings: (a) 38.0 g/cm^2 Cu, (b) 36.3 g/cm^2 Cu, (c) 30.3 g/cm^2 Cu, and (d) 32.3 g/cm^2 Cu. Solid lines represent observed numbers of events; broken lines represent the final estimate of the "true" momentum distribution.

(b) The particles travel in straight lines from the entrance plane toward the exit plane.

(c) The chamber is divided into 50 cells numbered from the entrance plane to the exit plane.

(d) Greek subscripts refer to the cells of the chamber, Latin subscripts to momentum intervals 25 Mev/c wide for both the incident momentum distribution discussed in Sec. I and the pathlength distribution.

The probabilities that particles from momentum bin i decay in cell α ($PD_{i\alpha}$), and that they interact in cell α ($PI_{i\alpha}$), were calculated from the following equations:

$$PD_{i\alpha} = m_{K^-} \left(\frac{\overline{1}}{P_{i\alpha}}\right) \frac{L/50}{c\tau_{K^-}} \left\{1 - \sum_{\beta=1}^{\alpha-1} (PD_{i\beta}+PI_{i\beta})\right\}, \qquad \text{(B-4)}$$

where

$\left(\frac{\overline{1}}{P_{i\alpha}}\right)$ = average value of $\frac{1}{P}$ in cell α for particles from bin i of the momentum distribution;

and

$$PI_{i\alpha} = A \left(\frac{\overline{1}}{P_{i\alpha}}\right) N \left\{1 - \sum_{\beta=1}^{\alpha-1} (PD_{i\beta}+PI_{i\beta})\right\}, \qquad \text{(B-5)}$$

where

A = constant to normalize the interaction cross section, and

N = number of protons/cc in the chamber.

Tracks whose residual range R at entrance was less than L had a probability of stopping given by

$$PS_{i\alpha} = 1 - \sum_{\beta=1}^{\alpha} (PD_{i\beta} + PI_{i\beta}), \qquad \text{(B-6)}$$

where α is the nearest integer $\leqslant [(50 \cdot R)/L] + 1$. When the particles had sufficient residual range to go through the chamber, the probability of being KGT was computed as

$$PGT_i = 1 - \sum_{\beta=1}^{50} (PD_{i\beta} + PI_{i\beta}) . \qquad (B-7)$$

Now that we have calculated the probabilities for K^- mesons terminating in the various cells α as a function of the momentum at entrance, we must calculate the pathlength contributed for each combination of incident momentum and termination cell. Consider a K^- entering the fiducial volume with momentum P. This K^- loses momentum as it penetrates the volume; we designate its momentum at various distances into the chamber by $q (q \leqslant P)$. At any point in the chamber, the residual range in hydrogen of the K^- is $R(q)$, and the amount of pathlength contributed between two momenta q_1 and q_2 is just $R(q_1) - R(q_2)$. Using this function $R(q)$, we construct a function $C_{n\alpha}(P)$, which gives the amount of pathlength contributed to the nth pathlength bin (momentum between $q_n - \Delta/2$ and $q_n + \Delta/2$) by a K^- that enters the fiducial volume with momentum P and terminates in cell α. Since we do not have the momentum of an individual particle at entrance, but a histogram of events, we must calculate the average pathlength $C_{ni\alpha}$ contributed by K^- mesons in bin i of the incident momentum distribution. This function is given in first approximation by

$$C_{ni\alpha} = \int_{P_i - \Delta/2}^{P_i + \Delta/2} C_{n\alpha}(P) \frac{dP}{\Delta} . \qquad (B-8)$$

We improve on this function by taking account of the slope of the momentum distribution of the incident K^- mesons. We then represent the momentum distribution of K^- over bin i by the simple function

$$D_i(P) = d_i^* + \frac{d_{i+1}^* - d_{i-1}^*}{2\Delta} (P - P_i) . \qquad (B-9)$$

When we weight the function $C_{n\alpha}(P)$ with $D_i(P)/d_i^*$, Eq. (B-8) becomes

$$C_{nia} = \int_{P_i-\Delta/2}^{P_i+\Delta/2} C_{na}(P) \left\{ 1 + \left(\frac{d_{i+1}^{*} - d_{i-1}^{*}}{2\Delta d_i^{*}} \right) (P-P_i) \right\} \frac{dP}{\Delta} , \tag{B-10}$$

where

$C_{na}(P)$ = pathlength contributed to nth pathlength bin by a K^- of momentum P terminating in cell a,

d_i^* = the number in bin i,

P_i = momentum at the center of bin i, and

Δ = 25 Mev/c.

Special account had to be taken of those bins for which the quantity in brackets went negative. The integral was cut off and the normalization $1/\Delta$ was changed accordingly.

The probabilities, the momentum distribution at entrance, and the quantities C_{nia} were used to calculate the pathlength distribution (C_n).

$$C_n = \sum_{i=1}^{15} d_i^* \left\{ C_{ni51}\ PGT_i + \sum_{a=1}^{50} C_{nia}(PD_{ia}+PI_{ia}+PS_{ia}), \right\} \tag{B-11}$$

where

d_i^* = number of K^- mesons in the ith momentum bin of the momentum distribution estimated in Subsection (1) above,

C_{nia} = pathlength contributed to nth pathlength bin by a K^- meson from momentum bin i, when it terminates in cell a ("cell 51" means all the way through the chamber).

The combined C_n from the four absorber settings is shown in Fig. 3.

The error in the pathlength was obtained by assuming a multinomial distribution for the events d_i^* in the momentum distribution, and propagating this through the equations given for pathlength. The variance-covariance matrix for the momentum distribution (i.e., for a multinomial distribution) is

$$\overline{\delta d_i^* \, \delta d_j^*} = d_i^* \left(\delta_{ij} - \frac{d_j^*}{N}\right) , \tag{B-12}$$

where

$$N = \sum_{i=1}^{15} d_i^* \simeq 11{,}000 .$$

Differentiating Eq. B-9 with respect to d_i^*, we get

$$\frac{\partial C_n}{\partial d_i} = \left\{ C_{n51i} \, PGT_i + \sum_{a=1}^{50} C_{nai} (PD_{ia} + PI_{ia} + PS_{ia}) \right\} \equiv F_{ni} . \tag{B-13}$$

Using the method of linear propagation of errors, we find for the error in the pathlength

$$\overline{\delta C_n \, \delta C_m} = \sum_{\substack{i=1 \\ j=1}}^{15} F_{ni} \, \overline{\delta d_i^* \, \delta d_j^*} \, F_{mj} . \tag{B-14}$$

This matrix was used to calculate the errors in cross sections discussed in Appendix C.

The numerical computations were done on an IBM 704 computer. The time for calculating the pathlength distribution for all four absorber settings was 45 minutes.

C. Variance-Covariance Matrices for the Cross Sections

The cross section in mb for a process averaged over momentum from $P_i-(\Delta/2)$ to $P_i+(\Delta/2)$ is given by

$$\sigma_n = \frac{K\, a_n'}{C_n} , \tag{C-1}$$

where

$K = 2.86 \cdot 10^4$ mb-cm = (number of protons/cc $\cdot\ 10^{-27})^{-1}$,

$a_n' = b_n a_n$,

a_n = maximum-likelihood estimate of the number of events with momentum between $P_i-(\Delta/2)$ and $P_i+(\Delta/2)$,

b_n = correction factor applied to the maximum-likelihood numbers for selection criteria, etc., and

C_n = pathlength (cm) between $P_i-(\Delta/2)$ and $P_i+(\Delta/2)$.

By propagating the uncertainties in a_n' and C_n linearly in Eq. C-1, we arrive at the following formula for the elements of the variance-covariance matrix for the cross sections:

$$\overline{\delta\sigma_m\ \delta\sigma_n} = \sigma_m\left(\frac{1}{a_m'}\ \overline{\delta a_m'\ \delta a_n'}\ \frac{1}{a_n'} - \frac{1}{C_m}\ \overline{\delta C_m\ \delta C_n}\frac{1}{C_n}\right)\sigma_n . \tag{C-2}$$

The variance-covariance matrix for the pathlength $\overline{\delta C_m\ \delta C_n}$ is discussed in Appendix B. The matrix $\overline{\delta a_m'\ \delta a_n'}$ is related to the variance-covariance matrix for the number of events as a function of momentum, $\overline{\delta a_m\ \delta a_n}$, by

$$\overline{\delta a_m'\ \delta a_n'} = b_n\ \overline{\delta a_m\ \delta a_n}\ b_n \tag{C-3}$$

The matrix $\overline{\delta a_m\ \delta a_n}$ is derived from the likelihood function for the number of events as a function of momentum.[4] This likelihod function is

$$L(\{P_o\}\,;\,a_p) = \frac{e^{-a}a^N}{N} \prod_{i=1}^{N} \sum_{n=1}^{15} \frac{a_n}{a} A_{ni}(P_{oi}), \qquad \text{C-4)}$$

where

$\{P_o\}$ = set of observed momenta, $P_{o1}, P_{o2}, \cdots, P_{oN}$,

a_n = true number of events in the nth momentum bin,

$a = \sum a_n$,

N = total number of observed events, and

$A_{ni}(P_o)$ = probability of the ith event's having an observed momentum P_o in the nth momentum bin.

Associated with the maximum-likelihood solution there is an estimate of the uncertainties given by the negative of the inverse of the second derivative of the logarithm of the likelihood function. Our final estimate of the uncertainty in the number of events $\overline{\delta a_n\ \delta a_m}$ is then

$$\overline{\delta a_n\ \delta a_m} = -\left(\frac{\partial^2 \ln L(\{P_o\}\,;\,a_p)}{\partial a_n\ \partial a_m}\right)^{-1} = \left(\sum_{i=1}^{N} \frac{A_{ni}\ A_{mi}}{\left(\sum_{P=1}^{15} a_p A_{pi}\right)^2}\right)^{-1}. \qquad \text{(C-5)}$$

Tables XI through XVI contain the variance-covariance matrices for the cross sections given in Table III (Sec. III-D). The uncertainties for the cross sections of Figs. 7 (elastic scattering) and 10 (charge-exchange scattering) are the square root of the diagonal terms of the matrices of Tables XV and XVI respectively.

Table XI

Variance-covariance matrix for the elastic-scattering cross section in the interval of cos $\theta_{c.m.}$ from -1.0 to 0.85 (see Table III for the cross sections)

K^- lab momentum intervals (Mev/c)	100-125	125-150	150-175	175-200	200-225	225-250	250-275
100-125	469.2	-10.0	-0.4	-0.6	-0.5	-0.5	-0.6
125-150	-10.0	168.2	-5.6	-0.1	-0.2	-0.4	-0.5
150-175	- 0.4	- 5.6	129.7	-2.6	-0.3	-0.4	-0.5
175-200	- 0.6	- 0.1	-2.6	61.2	-1.2	-0.0	-0.3
200-225	- 0.5	- 0.2	-0.3	-1.2	36.3	-1.7	-0.1
225-250	- 0.5	- 0.4	-0.4	-0.0	-1.7	42.5	-2.7
250-275	- 0.6	- 0.5	-0.5	-0.3	-0.1	-2.7	171.0

Table XII

Variance-covariance matrix for the elastic-scattering cross section in the interval of cos $\theta_{c.m.}$ from 0.85 to 0.90 (see Table III for the cross sections)

K^- lab momentum intervals (Mev/c)	100-125	125-150	150-175	175-200	200-225	225-250	250-275
100-125	30.4	-0.2	0.0	0.0	0.0	0.0	0.0
125-150	-0.2	9.9	0.0	0.0	0.0	0.0	0.0
150-175	0.0	0.0	3.8	0.0	0.0	0.0	0.0
175-200	0.0	0.0	0.0	3.4	0.0	0.0	0.0
200-225	0.0	0.0	0.0	0.0	1.2	0.0	0.0
225-250	0.0	0.0	0.0	0.0	0.0	2.3	0.0
250-275	0.0	0.0	0.0	0.0	0.0	0.0	28.2

Table XIII

Variance-covariance matrix for the elastic-scattering cross section in the interval of $\cos\theta_{c.m.}$ from 0.90 to 0.95 (see Table III for the cross sections)

K^- lab momentum intervals (Mev/c)	100-125	125-150	150-175	175-200	200-225	225-250	250-275
100-125	24.3	0.0	0.0	0.0	0.0	0.0	0.0
125-150	0.0	27.5	-0.4	0.0	0.0	0.0	0.0
150-175	0.0	-0.4	7.6	0.0	0.0	0.0	0.0
175-200	0.0	0.0	0.0	4.2	-0.2	0.0	0.0
200-225	0.0	0.0	0.0	-0.2	2.5	0.0	0.0
225-250	0.0	0.0	0.0	0.0	0.0	2.3	0.0
250-275	0.0	0.0	0.0	0.0	0.0	0.0	28.2

Table XIV

Variance-covariance matrix for the elastic-scattering cross section in the interval of cos $\theta_{c.m.}$ from 0.95 to 0.966 (see Table III for the cross sections)

K^- lab momentum intervals (Mev/c)	100-125	125-150	150-175	175-200	200-225	225-250	250-275
100-125	40.3	0.0	0.0	0.0	0.0	0.0	0.0
125-150	0.0	17.4	-0.2	0.0	0.0	0.0	0.0
150-175	0.0	-0.2	9.2	-0.8	0.0	0.0	0.0
175-200	0.0	0.0	-0.8	4.4	0.0	0.0	0.0
200-225	0.0	0.0	0.0	0.0	1.2	0.0	0.0
225-250	0.0	0.0	0.0	0.0	0.0	2.3	0.0
250-275	0.0	0.0	0.0	0.0	0.0	0.0	28.2

Table XV

Variance-covariance matrix for the elastic-scattering cross section in the interval of cos $\theta_{c.m.}$ from -1.0 to 0.966 (see Table III for cross sections)

K^- lab momentum intervals (Mev/c)	100-125	125-150	150-175	175-200	200-225	225-250	250-275
100-125	564.2	-10.2	-0.4	-0.6	-0.5	-0.5	-0.6
125-150	-10.2	223.0	-6.2	-0.1	-0.2	-0.4	-0.5
150-175	- 0.4	- 6.2	150.3	-3.4	-0.3	-0.4	-0.5
175-200	- 0.6	- 0.1	-3.4	73.2	-1.4	-0.0	-0.3
200-225	- 0.5	- 0.2	-0.3	-1.4	41.2	-1.7	-0.1
225-250	- 0.5	- 0.4	-0.4	-0.0	-1.7	49.4	-2.7
250-275	- 0.6	- 0.5	-0.5	-0.3	-0.1	-2.7	255.6

Table XVI

Variance-covariance matrix for the charge-exchange scattering cross sections of Table III

K^- lab momentum intervals (Mev/c)	89-125	125-150	150-175	175-200	200-225	225-250	250-275
89-125	470.0	-53.6	4.0	-0.4	0.0	0.0	0.0
125-150	-53.6	202.5	-16.2	1.4	-0.1	0.0	0.0
150-175	4.0	-16.2	125.2	-11.2	0.6	-0.3	0.0
175-200	-0.4	1.4	-11.2	54.1	-4.6	0.0	0.0
200-225	0.0	-0.1	0.6	-4.6	47.1	-10.8	0.0
225-250	0.0	0.0	-0.3	0.0	-10.8	81.4	0.0
250-275	0.0	0.0	0.0	0.0	0.0	0.0	144.5

FOOTNOTES AND REFERENCES

1. S. C. Freden, C. Gilbert, and R. S. White, Phys. Rev. 118, 564 (1960).
2. P. Nordin, A. H. Rosenfeld, F. T. Solmitz, R. D. Tripp, and M. B. Watson, Bull. Am. Phys. Soc. 4, 288 (1959).
3. Luis W. Alvarez, The Interactions of Strange Particles, Lawrence Radiation Laboratory Report UCRL-9353, Aug. 11, 1960. This report is a copy of the "rapporteur talk" given by Luis W. Alvarez at the 1959 Kiev Conference on High-Energy Physics. The report of the Proceedings of the Kiev Conference is not yet available in published form.
4. William E. Humphrey, Hyperon Production by K^- Mesons Incident on Hydrogen (Ph. D. Thesis), Lawrence Radiation Laboratory Report UCRL-9752, June 1961 (unpublished).
5. Joseph J. Murray, A Coaxial Static-Electromagnetic Velocity Spectrometer for High-Energy Particles, University of California Radiation Laboratory Report UCRL-3492, May 1957 (unpublished).
6. N. Horwitz, J. J. Murray, R. R. Ross, and R. D. Tripp, 450-Mev/c K^- and $\bar{p}$ Beams at the Northwest Target Area of the Bevatron Separated by the Coaxial Velocity Spectrometer, University of California Radiation Laboratory Report UCRL-8269, June 1958 (unpublished).
7. A. H. Rosenfeld, Proceedings of the International Conference on High-Energy Accelerators and Instrumentation (CERN, Geneva, 1959), pp 533-541. For a more detailed description of program PANG, see William E. Humphrey, A Description of the PANG Program, Alvarez Group Physics Memos 111 and 115, Lawrence Radiation Laboratory, Berkeley (unpublished).
8. A. H. Rosenfeld and J. N. Snyder, Digital-Computer Analysis of Data from Bubble Chambers. IV. The Kinematical Analysis of Complete Events, Lawrence Radiation Laboratory Report UCRL-9098, February 16, 1960.

9. H.A. Bethe, Phys. Rev. 89, 1256 (1953).

10. Walter H. Barkas and Arthur H. Rosenfeld, Data for Elementary-Particle Physics, University of California Radiation Laboratory Report UCRL-8030, March 20, 1958 (unpublished).

11. J.D. Jackson, D.G. Ravenhall, and H.W. Wyld, Nuovo cimento 10, 9, 834 (1958).

12. R.H. Dalitz, Strange-Particle Interactions, in Proceedings of the 1958 Annual International Conference on High-Energy Physics (CERN, Geneva, 1959), pp. 187-201.

13. J.D. Jackson and H.W. Wyld, Nuovo cimento 10, 13, 85 (1959); Phys. Rev. Letters 2, 355 (1959).

14. R.H. Dalitz and S.F. Tuan, Ann. Phys. 3, 307 (1960).

15. T.B. Day, G.A. Snow, and J. Sucher, Phys. Rev. Letters 3, 61 (1959).

16. R.H. Dalitz, On the Strong Interactions of the Strange Particles, Lawrence Radiation Laboratory Report UCRL-9580, January 27, 1961 (unpublished).

17. Ulrich Kruse and Michael Nauenberg, S-Wave K^--N Scattering Amplitudes, Lawrence Radiation Laboratory Report UCRL-8888, September 11, 1959 (unpublished).

18. See, for instance: Harold Cramér, The Mathematical Methods of Statistics, (Princeton University Press, Princeton, 1946) p. 416 ff.

19. J. Peter Berge, Frank T. Solmitz, and Horace D. Taft, Rev. Sci. Instr. 32, 538 (1961).

20. The systematic shift of the mean of one of these distributions can have serious effects on the analysis of events if it represents a large enough absolute change in the corresponding physical variable. However, in the case of S(k) for the proton (whose mean deviates most significantly from zero), the shift in the mean corresponds to a systematic error in the momentum of the proton (measured from range) of less than 1 Mev/c, and has a negligible effect on the corresponding energy in the K^--p system. All other systematic shifts also have negligible effects on the K^--p system.

This report was prepared as an account of Government sponsored work. Neither the United States, nor the Commission, nor any person acting on behalf of the Commission:

A. Makes any warranty or representation, expressed or implied, with respect to the accuracy, completeness, or usefulness of the information contained in this report, or that the use of any information, apparatus, method, or process disclosed in this report may not infringe privately owned rights; or

B. Assumes any liabilities with respect to the use of, or for damages resulting from the use of any information, apparatus, method, or process disclosed in this report.

As used in the above, "person acting on behalf of the Commission" includes any employee or contractor of the Commission, or employee of such contractor, to the extent that such employee or contractor of the Commission, or employee of such contractor prepares, disseminates, or provides access to, any information pursuant to his employment or contract with the Commission, or his employment with such contractor.